Research Square

Preprints are preliminary reports that have not undergone peer review.
They should not be considered conclusive, used to inform clinical practice,
or referenced by the media as validated information.

Marine Heatwave-Induced Stratification Promoted Subsurface Heat Storage and Supported the Rapid Intensification of Tropical Cyclone Winston

Matthew Chinappa

matthewchinappa@gmail.com

University of the South Pacific - Laucala Campus: The University of the South Pacific
https://orcid.org/0000-0002-8264-1201

Alexandre Ganachaud

Université de Toulouse: Universite de Toulouse

Awnesh Singh

University of the South Pacific - Laucala Campus: The University of the South Pacific

Saurabh Rathore

Indian Institute of Technology Delhi

Research Article

Keywords: marine heatwaves, tropical cyclone rapid intensification, mixed-layer stratification, mixed layer heat reservoir, ocean–atmosphere coupling

Posted Date: July 6th, 2026

DOI: https://doi.org/10.21203/rs.3.rs-10159406/v1

License: This work is licensed under a Creative Commons Attribution 4.0 International License.
Read Full License

Marine Heatwave-Induced Stratification Promoted Subsurface Heat Storage and Supported the Rapid Intensification of Tropical Cyclone Winston

Matthew Chinappa*,[1,] Alexandre Ganachaud,[2,3,4] Awnesh Singh,[1] Saurabh Rathore[5]

[1]Centre for Sustainable Futures, The University of the South Pacific, Suva, Fiji
[2]IRD, Université de Toulouse, UMR5566 – LEGOS, Toulouse, France
[3]IRD, Université de Montpellier, UMR248 – MARBEC, Sète, France
[4]IRD, Noumea Center, New Caledonia
[5]Centre for Atmospheric Sciences, Indian Institute of Technology Delhi

*Corresponding author: Matthew Chinappa, matthewchinappa@gmail.com

Abstract

Marine heatwaves (MHWs) are increasingly recognized as modulators of tropical cyclone (TC) intensity, yet the mechanisms linking upper-ocean preconditioning to rapid intensification (RI) remain incompletely understood. Here, we investigate the coupled ocean–atmosphere processes associated with the rapid intensification of Tropical Cyclone Winston (2016) during an extreme MHW in the southwest Pacific. Observational, reanalysis, and high-resolution ocean-model diagnostics show that sustained radiative forcing and weak surface winds generated a shallow mixed layer (~13–17m) and enhanced upper-ocean stratification, promoting substantial heat accumulation in the upper ocean. Mixed-layer heat budget analysis reveals that much of the surface heat input was redistributed beneath the mixed layer rather than retained locally, producing a vertically structured thermal reservoir extending into the upper thermocline. During Winston's rapid intensification, storm-induced mixing progressively accessed this stored heat, with cooling and heat-content depletion extending well below the pre-storm mixed-layer depth. The strongest heat-content reductions occurred within subsurface reservoirs (300-600 m) rather than within the mixed layer itself, demonstrating that the energetically important oceanic response was concentrated beneath the surface layer. Despite substantial ocean heat loss, elevated turbulent heat fluxes were maintained, consistent with entrainment of anomalously warm subsurface waters that reduced the cooling typically associated with deep mixing. Rapid intensification occurred when elevated upper-ocean heat availability coincided with weak vertical wind shear (VWS) and enhanced ocean-to-atmosphere energy transfer. The contribution of MHWs to TCs intensification extends beyond elevated sea-surface temperatures and involves modification of the vertical distribution and accessibility of upper-ocean heat. The study highlights the importance of subsurface thermal structure for tropical cyclone intensification and demonstrates the value of coupled ocean–atmosphere diagnostics for understanding compound MHW–TC extremes in the data-limited southwest Pacific.

KEYWORDS

marine heatwaves; tropical cyclone rapid intensification; mixed-layer stratification; mixed layer heat reservoir; ocean–atmosphere coupling

1. Introduction

Tropical cyclones (TCs) are among the most destructive natural hazards, deriving their energy from the enthalpy fluxes of the warm upper ocean (K. Emanuel, 1985; K. A. Emanuel, 1999). TCs affect Fiji primarily during the Southern Hemisphere cyclone season from November to April, although events may occasionally occur in October and May during El Niño years. Between the 1969/70 and 2017/18 seasons, a total of 135 tropical cyclones passed within the Fiji Exclusive Economic Zone (EEZ). Despite substantial interannual variability, there has been little change, or a marginal decline, In the total number of tropical cyclones over the past four decades (McGree et al., 2023).

TC Winston (Figure 1), a highly destructive Category 5 cyclone, made landfall in Fiji on Saturday, February 20, 2016. The event marked the first time a Category 5 cyclone directly affected Fiji and was the countr''s most intense cyclone ever recorded. The initial impact occurred in Fij''s Eastern Division, causing severe damage to Koro, Ovalau, and Taveuni Islands (Figure 1). As the cyclone traversed Fij''s islands, it reached its peak intensity just before making landfall on the island of Viti Levu, the largest island. Winston ranked among the Southern Hemispher''s most potent cyclones, with maximum average wind speeds reaching 233 km hr^{-1} and gusts peaking at approximately 306 km hr^{-1}. In addition to the extreme wind speeds, storm surges extended almost 200 meters inland in some areas' TC Winston created widespread damage and destruction, impacting around 540,400 people, equivalent to 62 per cent of the countr''s total population. The estimated value of the disaster effects resulting from TC Winston in Fiji amounted to US$D0.9 billion, encompassing USD$0.6 billion in damage (i.e., destroyed physical assets) and USD$0.3 billion in losses (Esler, 2016).

A growing body of research indicates that MHWs can enhance tropical cyclone intensity by creating exceptionally warm ocean conditions that favour storm development and intensification (Balaguru et al., 2015, 2016; Rathore et al., 2022; Radfar et al., 2024; Choi et al., 2024a; Nguyen & Hsu, 2025; Han et al., 2025; Pun et al., 2025). For example, Rathore et al. (2022) showed that the rapid intensification of Cyclone Amphan in the Bay of Bengal coincided with a strong MHW and anomalously high upper-ocean heat content, highlighting the importance of oceanic thermal conditions in supporting extreme cyclone intensification. Similar links between MHWs and enhanced TC intensity have been documented across multiple ocean basins, suggesting that these events provide a favourable oceanic environment for storm strengthening. Extending these regional findings, Choi et al. (2024) showed from a global analysis that TCs interacting with MHWs exhibit intensification rates and peak intensities approximately 30–40% higher, on average, than storms developing over non-MHW waters. These responses are thought to arise from increased ocean-to-atmosphere energy transfer, including enhanced latent heat fluxes and

atmospheric moisture availability, which sustain cyclone intensification (Emanuel, 1999; Balaguru et al., 2012; Lin et al., 2013).

A key mechanism linking MHWs to enhanced TC intensification is the presence of increased stratification, which can maintain a reservoir of anomalously warm water beneath the surface (Balaguru et al., 2012; Oliver et al., 2017). Such conditions reduce the entrainment of cooler thermocline water during storm passage and suppress TC-induced sea-surface temperature (SST) cooling, thereby sustaining the ocean-to-atmosphere heat and moisture fluxes that fuel cyclone intensification (Goni & Trinanes, 2003; Price, 1981; Shay et al., 2000). Balaguru et al. (2012) further showed that salinity-induced barrier layers can enhance this process by isolating warm subsurface water beneath the mixed layer, reducing vertical mixing and preserving the upper-ocean heat reservoir available to a storm. This reduction in storm-induced surface cooling, often referred to as cold-wake mitigation, enables tropical cyclones to maintain stronger air–sea coupling and has been identified as an important factor supporting rapid intensification, particularly in environments that are only marginally favourable for cyclone development (Jaimes & Shay, 2015; Li et al., 2021; Lin et al., 2009a; Vincent et al., 2015).

In early 2016, an intense MHW developed over Fiji's Exclusive Economic Zone (Holbrook et al., 2022) establishing a highly favorable thermodynamic environment prior to the rapid intensification of TC Winston. Dutheil et al. (2024) show that the extreme 2016 Southwest Pacific MHW was not driven by El Niño alone, but by a compound interaction between a strong Madden–Julian Oscillation (MJO) and an extreme El Niño, which together suppressed convection, reduced winds, increased shortwave radiation, and weakened latent heat loss, leading to rapid upper-ocean warming. Their heat budget analysis demonstrated that anomalous surface heat fluxes—particularly enhanced solar radiation and reduced evaporative cooling—dominated the heat accumulation phase, while ocean dynamics played a secondary role during growth. The event then ended abruptly when Tropical Cyclone Winston induced strong vertical mixing and enhanced latent heat loss, rapidly cooling the ocean. Overall, they conclude that the life cycle of the heatwave reflects nonlinear interactions between large-scale climate modes and synoptic events, rather than a single forcing mechanism.

In this study, we investigate the oceanic processes linking marine heatwave (MHW) preconditioning to the rapid intensification (RI) of Tropical Cyclone Winston. Using observations, ocean reanalysis products, atmospheric reanalysis fields, and high-resolution ocean-model diagnostics, we first examine how the 2016 southwest Pacific MHW altered upper-ocean structure through enhanced radiative forcing, mixed-layer shoaling, and increased stratification. We then quantify how these processes promoted the accumulation and persistence of heat within and beneath the mixed layer, creating a vertically structured upper-ocean heat reservoir prior to cyclone passage. Finally, we examine how Winston interacted with this preconditioned ocean state through analyses of upper-ocean thermal evolution, heat-content depletion, and ocean–atmosphere energy

exchange during rapid intensification. By linking the formation, storage, and subsequent utilization of upper-ocean heat, this study provides a mechanistic framework for understanding how marine heatwaves can influence tropical cyclone intensification through modifications to the vertical distribution and accessibility of ocean heat. These findings provide insight into a historic southwest Pacific extreme event and highlight the growing importance of compound MHW–TC interactions in a warming climate.

The paper is structured as follows. Section 2 describes the datasets and methodology. Section 3.1 evaluates the reliability of the observational, reanalysis, and model products used in the study. Section 3.2 examines the oceanic preconditioning associated with the marine heatwave, including the evolution of SST, surface heat fluxes, upper-ocean thermal structure, stratification, and heat storage. Section 3.3 investigates the evolution of this stored heat during Tropical Cyclone Winston's rapid intensification through analyses of along-track thermal structure, heat-content depletion, and coupled ocean–atmosphere energy exchange. Section 4 discusses the implications of these results for tropical cyclone–ocean interactions and compound climate extremes, and Section 5 summarizes the principal conclusions.Click or tap here to enter text.

2. Data and Methodology

2.1 Data

2.1.1 Atmospheric and Sea Surface Data

Daily Optimum Interpolation Sea Surface Temperature (OISST) Version 2 data at 0.25° spatial resolution (Huang et al., 2021) were obtained from the National Oceanic and Atmospheric Administration (NOAA) for the period 1982–2020. OISST was used for the detection and characterization of marine heatwave (MHW) events.

Atmospheric variables were obtained from the ERA5 reanalysis (Hersbach et al., 2020) produced by the European Centre for Medium-Range Weather Forecasts (ECMWF). ERA5 provides hourly global fields at 0.25° spatial resolution from 1950 to the present. Variables used in this study included sea surface temperature, surface heat fluxes (shortwave radiation, longwave radiation, latent heat flux, and sensible heat flux), and wind components at multiple pressure levels. ERA5 SST fields were used as atmospheric forcing within the ocean model simulations, while OISST was used exclusively for MHW identification.

Hourly 10-m wind fields (u10 and v10) were obtained from ERA5 and corrected using the parametric–reanalysis wind reconstruction method of Herry et al. (2025) to account for the underrepresentation of tropical cyclone core winds in coarse-resolution reanalysis products. The method combines a best-track-constrained parametric vortex with the large-scale ERA5 environmental flow, preserving realistic storm structure and asymmetry while maintaining consistency with the surrounding synoptic environment. Reconstructed winds were sampled along

tropical cyclone tracks and used to calculate surface kinetic energy and its temporal tendency, providing a physically consistent measure of atmospheric energy evolution during rapid intensification.

2.1.2 Subsurface Ocean Data

Subsurface ocean conditions were obtained from the Global Ocean Reanalysis and Simulation (GLORYS2V4) product (Global Ocean Ensemble Physics Reanalysis, Product ID: GLOBAL_MULTIYEAR_PHY_ENS_001_031) developed by Mercator Ocean International (Garric & Parent, 2016). GLORYS2V4 is an eddy-permitting global ocean reanalysis that provides daily fields of temperature, salinity, and ocean currents on a 0.25° horizontal grid with 50 vertical levels spanning the period 1993–2020. The reanalysis assimilates a wide range of satellite and in situ observations, providing a physically consistent representation of the three-dimensional ocean state. To resolve sub-daily upper-ocean variability, the daily GLORYS2V4 profiles were used to initialize simulations with the Coastal and Regional Ocean Community model (CROCO). The model was forced with hourly atmospheric fields from ERA5, allowing the evolution of the upper ocean in response to realistic meteorological conditions. Hourly ocean fields were generated to a depth of 120 m, enabling representation of diurnal warming, vertical mixing, entrainment, and mixed-layer variability that are not resolved by the daily reanalysis. Consistency with the parent reanalysis was maintained, with daily averages of the hourly model output closely reproducing the corresponding GLORYS2V4 fields. The hourly CROCO output was subsequently used to derive mixed-layer depth and other upper-ocean diagnostics examined in this study.

2.1.3 Tropical Cyclone Data

The Southwest Pacific Enhanced Archive for Tropical Cyclones (SPEArTC; http://apdrc.soest.hawaii.edu/projects/speartc/) was used to obtain the best track data for Tropical Cyclone (TC) Winston (Knapp et al., 2010). This dataset records of TC position (latitude, longitude), maximum sustained wind speed (ms^{-1}), and central pressure (hPa).

2.2 Methods

2.21 Validating Open Ocean and Local Data

We assessed CMEMS GLORYS, NOAA OISST, and ERA5 SST fields against independent in-situ observations from Argo profiling floats and fixed reef temperature loggers (Le Gendre et al., 2025) in the South Pacific for 1 January–29 February 2016. Argo profiles (0–200m) and surface temperatures (from the shallowest valid measurement, typically ~2-4m) were quality-controlled using standard delayed-mode flags. Reef temperatures were obtained from six loggers deployed at 10–15m depth. Each dataset was spatially and temporally collocated with the nearest in-situ observation using a ±0.1° radius and daily matching. Performance was quantified using bias,

RMSE, MAE, correlation, and the spread of individual-instrument errors. Where systematic offsets were identified, simple additive bias-correction terms were derived to harmonize products with observational baselines.

2.22 Marine Heatwave Detection

MHWs were identified using the established definition of (Hobday et al., 2016, 2018), implemented with the R package heatwaveR (W. Schlegel & J. Smit, 2018). For each grid cell in the study region, a daily climatology and the 90th percentile threshold were calculated for the baseline period 1993–2016. A MHW was defined as a period of at least five consecutive days where the daily SST exceeded the seasonally varying 90th percentile threshold. To ensure event coherence, gaps of two days or less where SST dropped below the threshold were allowed, merging the periods into a single, prolonged MHW event.

2.23 Mixed Layer Heat Budget (MLHB)

The MLHB (Moisan & Niiler, 1998) was used to diagnose the physical processes governing the upper ocean temperature tendency. The budget is expressed as:

$$\frac{\partial T}{\partial t} = -\left(\frac{1}{h}\right)\left[\int_0^h u\left(\frac{\partial T}{\partial x}\right)dz + \int_0^h v\left(\frac{\partial T}{\partial y}\right)dz\right] + \frac{(Q_{Net} - Q_{Penetr})}{\rho\, C_p h} + Res \qquad (1.1)$$

Where:

T is temperature, Q_{Net} is the net air-sea heat flux, ρ_0 is seawater density, C_p is specific heat capacity, h is the mixed layer depth, R is a combination of all the mixing terms and horizontal ocean currents are represented by u and v. The net surface heat flux reaching the sea surface (Q_{Net}) can be decomposed into turbulent fluxes—the sum of latent heat flux (Q_{lh}) and sensible heat flux (Q_{sh})—and radiative components: the sum of net surface shortwave radiation Q_{sw}, which is incoming solar radiation minus the outgoing reflected shortwave due to albedo) and net surface longwave radiation (Q_{lw}):

$$Q_{Net} = Q_{sw} + Q_{lw} + Q_{lh} + Q_{sh} \qquad (1.2)$$

A portion of Q_{sw} penetrates beyond the base of the mixed layer. The penetrating radiative flux (Q_h) is calculated following Paulson & Simpson (1977), using two extinction lengths for Jerlov water type 1A/1B:

$$Q_h = Qsw[R \cdot e^{-\frac{h}{\xi 0}} + (1 - R) \cdot e^{-\frac{h}{\xi 1}}] \qquad (1.3)$$

where h is the layer depth from the surface to base of the mixed layer depth, R = 0.62, $\xi 0$ = 1.0 m, and $\xi 1$ = 20 m. Therefore, the shortwave radiation absorbed within the layer h is $Q_{sw} - Q_h$. The complete MLHB is defined as a combination Equations 1.1, 1.2 and 1.3.

2.24 The Tropical cyclone Heat Potential (TCHP)

Hereafter referred to as OHC D26 was computed to understand the effect of ocean heat accumulation for the compound extreme event of MHW and tropical cyclone. The OHC D26 is defined using Equation 2:

$$\mathrm{THCP} = \int_0^{\mathrm{D_h}} \rho\, \mathrm{C_p}(\mathrm{T(z)} - \mathrm{T(26)}\mathrm{dz} \qquad (2)$$

where ρ is the ocean density, Cp is specific heat capacity, D_{26} is the depth of the 26˚C isotherm in the ocean and T is the reference temperature at depth (Leipper & Volgenau, 1972).

2.25 Stratification strength: Brunt–Väisälä frequency (N^2)

Vertical stability was estimated from temperature and salinity profiles obtained from GLORYS2V4 reanalysis. Seawater density (ρ) was computed using the TEOS-10 equation of state (McDougall & Barker, 2011). The Brunt–Väisälä frequency (N^2; s^{-2}) was calculated as:

$$N^2 = -\frac{g}{\rho_0}\frac{\partial \rho}{\partial z} \qquad (3)$$

Where g=9.81ms^{-2} and ρ_0=1025kgm^{-3}. Vertical density gradients were obtained using centered finite differences between 1 m vertical levels. N^2 values were averaged over the upper 50 m to characterize near-surface stratification. Mean N^2 values were computed for pre-MHW (1 Jan–14 Feb 2016) and MHW (15–29 Feb 2016) periods. An increase in mean N^2 indicated enhanced stratification and reduced mixing potential prior to the heatwave onset. N^2 is defined as Equation 3.

2.2.6 Oceanic Heat Content and Excess Energy Calculation

Mixed Layer heat content anomaly (*OHC'*) and its persistence against surface cooling were analyzed in the region traversed by TC Winston (176–183°E, 17–20°S) during the 2016 MHW. Daily potential temperature and mixed-layer depth were obtained from the CMEMS GLORYS12V1 global ocean reanalysis (0.25° horizontal resolution, 0–1400 m depth). Temperature anomalies (ΔT(z)) were computed relative to a 1993–2016 daily climatology (grouped by day-of-year). The OHC anomaly was then calculated at every grid point by vertically integrating the temperature anomaly from the surface to the daily mixed-layer depth (MLD) using the trapezoidal rule. The resulting gridded OHC anomalies were subsequently spatially averaged over the study domain to produce a regional mean time series representing the evolution of upper-ocean thermal energy during the study period.

$$OHC' = \rho_0 C_p \int_0^{MLD} \Delta T\,(z)dz \qquad (4)$$

where ρ_0 = 1025 kg m^{-3} and C_p = 3990 J kg^{-1} °C^{-1}. OHC' forms a heat *reservoir*. All quantities were spatially averaged over the study box (Section 3.2.1) to produce regional-mean time series. Surface heat fluxes were taken from ERA5 (hourly, 0.25° resolution). Latent and sensible heat fluxes (`$F_{LH}$` and `$F_{SH}$`) were converted from accumulated values to instantaneous rates (W m^{-2}) and sign-adjusted so that positive values indicate ocean heat loss to the atmosphere. The equivalent turbulent flux timescale (t_{eq}) quantifies mixed layer heat reservoir persistence as:

$$t_{eq} = \frac{OHC'}{(F_{LH} + F_{SH}) * 86400 s/day} \qquad (5)$$

calculated only when turbulent flux > 0 (ocean losing heat). This metric represents the number of days (86,400 seconds) of observed turbulent cooling required to remove the existing OHC anomaly. The 75th percentile threshold was selected to identify sustained elevated heat-content anomaly conditions. The objective is to characterize the persistence of the upper-ocean mixed layer heat reservoir relevant to tropical cyclone preconditioning. Given the shallow mixed-layer depth (~10–16 m), the distribution of OHC anomalies is inherently constrained, such that higher percentiles (90th–95th) yield a small number of transient peaks that do not represent sustained heat storage. The 75th percentile instead captures a broader regime of elevated OHC anomaly conditions, which are more relevant for assessing the persistence of ocean heat content and its interaction with atmospheric forcing, as quantified by the equivalent flux timescale t_{eq}.
To represent the thermodynamic effect of OHC' we convert it into an equivalent temperature anomaly using: $\Delta Teq = \frac{OHC'}{\rho cph}$.

2.27 Vertical Wind Shear (VWS)

Vertical wind shear (VWS), a key environmental parameter influencing tropical cyclone development and intensification, was calculated from ERA5 daily mean zonal (u) and meridional (v) wind components as the magnitude of the vector wind difference between 200 and 850 hPa:

$$VWS = \sqrt{(u_{200} - u_{850})^2 + (v_{200} - v_{850})^2} \qquad (6)$$

where u_{200} and u_{850} are the zonal wind components at 200 and 850 hPa, respectively, and v_{200} and v_{850} are the corresponding meridional wind components. VWS was first calculated at each ERA5 grid point and subsequently averaged over the study domain to obtain a regional mean shear time series. No storm-centered averaging or vortex-removal procedure was applied.

2.28 Track-Based Energy Budget Diagnostics

Environmental diagnostics were derived by combining multiple datasets sampled along the TC Winston track. THCP was calculated from hourly ocean reanalysis temperature profiles using the depth-integrated heat content above the 26°C isotherm. Turbulent surface heat fluxes Q_{turb} and near-surface atmospheric winds were obtained from hourly ERA5 reanalysis fields and extracted at the storm position at each analysis time. Atmospheric kinetic energy (KE) for the phase-composite analysis was estimated from best-track maximum sustained wind speed as ($KE = \frac{1}{2} V_{max}^2$) providing a storm-scale measure of cyclone intensity. In contrast, the hourly KE tendency shown in Figure 8A was derived from ERA5 near-surface winds to characterise short-term variations in the local atmospheric energy field surrounding the cyclone.

Temporal tendencies were calculated using centred finite differences. Hourly tendencies of KE, THCP, and Q_{turb} were computed from the hourly track and used to examine short-timescale variability in air–sea energy exchange (Figure 8A–C). Environmental evolution and phase-composite analyses (Figure 8D–E) were evaluated using the 6-hourly best-track record to maintain consistency with the cyclone intensity dataset. To facilitate comparison among variables with different units and magnitudes, the environmental variables shown in Figure 8D–E were standardised using z-score anomalies computed relative to the mean and standard deviation over the analysis period.

2.3 Study Region

Fiji is a tropical Southwest Pacific archipelago comprising over 330 islands within an Exclusive Economic Zone of approximately 1.29 million km². The islands are situated on a raised submarine plateau generally shallower than 2,000 m, which extends southward as the Lau Ridge and is surrounded by deep ocean basins exceeding 6,000 m. Approximately 97% of Fiji's waters are deeper than 200 m, with a mean depth of ~2,700 m, indicating a predominantly deep-ocean environment. The regional bathymetry is highly complex, featuring ridges, seamounts, plateaus and submarine canyons. At least 59 seamounts and several ridge systems (e.g., Lau, Colwyn and Denham ridges) rise thousands of metres above the abyssal plains, strongly influencing circulation and vertical structure. Fiji lies along the Pacific Ring of Fire, with active tectonics expressed through earthquakes, submarine volcanism and hydrothermal systems, particularly within the Lau Basin. These processes play a key role in shaping seafloor morphology and regional ocean structure. Surface circulation is dominated by the westward-flowing South Equatorial Current, strongest north of the main islands, which interacts with island topography to generate zonal jets and spatially variable mixing. Surface salinity is relatively uniform (34.6–35.6 PSU), with a stratified upper ocean characterised by a pronounced halocline. The mixed layer depth ranges from ~26 to 47 m (mean ~37 m), with shallower layers to the south and east and deeper layers to the north, consistent with enhanced mixing associated with stronger current flow (Gassner et al., 2019). TC Winston intensified over anomalously warm waters, reaching Category 5 intensity immediately prior to landfall on Viti Levu. The analysis therefore focuses on a broader region

encompassing Fiji and the ocean to its east (176–183°E, 17–20°S), where Tropical Cyclone Winston underwent rapid intensification to Category 5 prior to landfall.

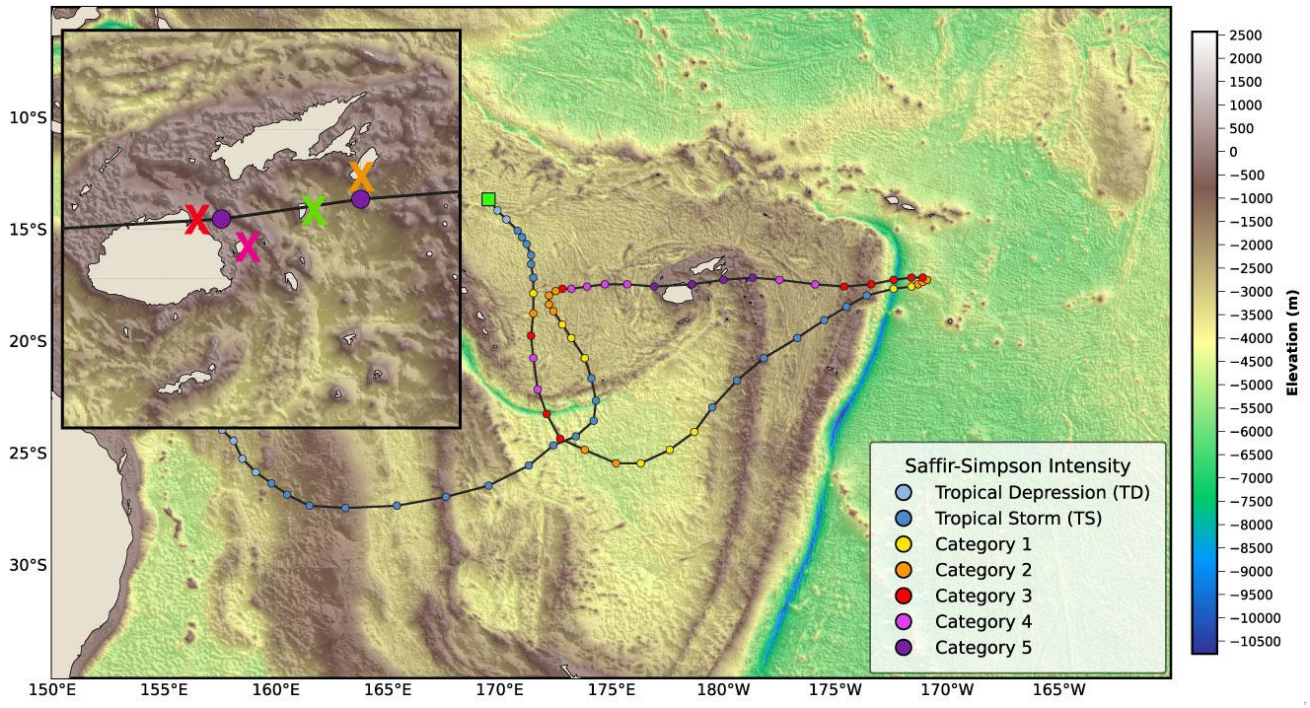


Figure 1 Bathymetric context for TC Winston (2016) in the southwest Pacific Ocean. Gridded bathymetry reveals the large-scale oceanic setting through which Winston travelled prior to and during rapid intensification. The colors represent the storm's maximum sustained wind speeds as classified in the Saffir–Simpson scale (see below), and the shape of the data points represent the nature of the storm, according to the legend below. Saffir–Simpson scale. Tropical depression (≤38 mph, ≤62 km/h), Tropical storm (39–73 mph, 63–118 km/h), Category 1 (74–95 mph, 119–153 km/h), Category 2 (96–110 mph, 154–177 km/h), Category 3 (111–129 mph, 178–208 km/h), Category 4 (130–156 mph, 209–251 km/h), Category 5 (≥157 mph, ≥252 km/h). The zoomed inset panel in the top left shows the most affected areas, denoted by X markers. The orange X indicates Taveuni, the green X indicates Koro, and the red X on the northeastern coast of Viti Levu marks the location where Tropical Cyclone Winston made landfall shortly before reaching peak intensity.

3. Results

We first evaluate the performance of the observational, reanalysis, and model datasets used in this study. We then examine the oceanic preconditioning associated with the 2016 MHW, including changes in surface forcing, upper-ocean thermal structure, stratification, and heat storage. Finally, we investigate how this preconditioned ocean state interacted with TC Winston during rapid intensification through analyses of along-track thermal evolution, heat-content depletion, and ocean–atmosphere energy exchange.

3.1 Validating Open Ocean and Local Data

Validation against independent observations demonstrates that the selected ocean datasets provide a realistic representation of thermal conditions in the Fiji region during the study period. GLORYS2V4 was evaluated against 58 quality-controlled Argo temperature profiles over the

common depth range available in both datasets (surface to approximately 1500 m). For each profile, GLORYS2V4 temperatures were collocated in space and time and linearly interpolated onto the observed Argo pressure levels prior to comparison. Across 14,211 collocated temperature measurements, GLORYS2V4 exhibited a mean bias of −0.18 °C, RMSE of 0.64 °C, MAE of 0.41 °C, and a correlation coefficient of 0.997, indicating excellent agreement with observed upper-ocean and subsurface temperature structure. OISSTV2 also compared favourably with near-surface Argo observations (2–7 m depth), yielding a mean bias of +0.32 °C, RMSE of 0.72 °C, and correlation coefficient of 0.74 across 58 collocations. Independent validation against seven reef temperature logger records further demonstrated the accuracy of OISSTV2, with a mean bias of +0.16 °C, RMSE of 0.40 °C, and correlation coefficient of 0.97. Consequently, the original datasets were retained for analysis.

3.2 Oceanic Preconditioning by the MHW

3.2.1 Persistent MHW Conditions, SST and Surface Wind Evolution

TC Winston evolved within a region of highly persistent MHW conditions, with MHW frequency exceeding 80–100% relative to the 1993–2016 baseline across a broad area between ~176–183°E and 17–20°S during 27 January–14 February 2016 (Figure 2a, white rectangle). Within the boxed region, MHW conditions were effectively continuous (>90% of days), indicating that the upper ocean remained above the seasonally varying 90th percentile threshold throughout the preconditioning and intensification phases of the storm. Surrounding regions show a sharp gradient in persistence (dropping to <40–60% east of ~185°E), highlighting that the cyclone track was preferentially aligned with the core of the warm anomaly field rather than its periphery. The MLD, indicated by black contours, varies spatially between approximately ~13m and ~25m. Shallower mixed layers (~13–17m) are co-located with regions of highly persistent MHW conditions in the mid central portions of the domain. Deeper mixed layers (~19–25m) occur toward the eastern region and along localized contour maxima. Surface wind vectors (cyan) show relatively weak magnitudes across much of the domain, with typical vector lengths corresponding to <5 ms^{-1} (as indicated by the reference arrow). Wind direction is predominantly westward to southwestward across the central region, with localized directional variability near the cyclone track.

Area-averaged SST anomalies (Figure 2B) increased from approximately −0.5 °C in early January to ~2.0–2.1 °C by 8–10 February, corresponding to the MHW onset phase. This warming occurred under relatively weak wind conditions ($|U| \lesssim 3–5$ ms^{-1} prior to ~25 January). During the MHW period (27 January–14 February), SST anomalies remained persistently elevated (≥1.5°C for ~10–12 consecutive days), indicating sustained positive upper-ocean heat content rather than short-lived atmospheric forcing. As TC Winston intensified (mid-February), wind speeds increased rapidly to ~7–8 ms^{-1}, yet SST anomalies remained elevated (>1°C). Following the cyclone passage (~15 February), SST anomalies declined sharply from ~1.5 °C to <0 °C within ~5–7 days is

consistent with enhanced vertical mixing and entrainment of cooler, upper thermocline waters driven by strong winds (Vincent et al., 2013).

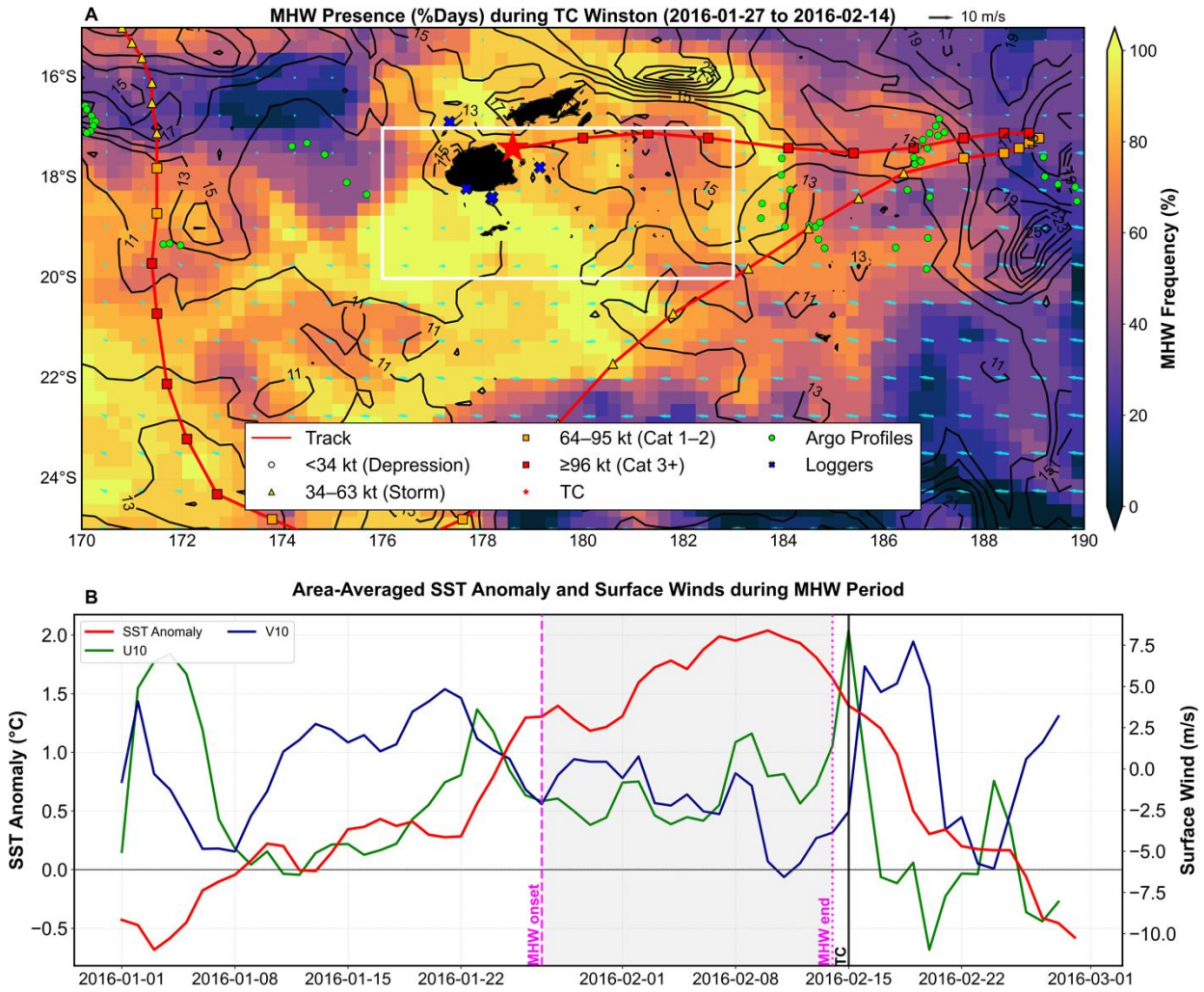


Figure 2 MHW Presence during TC Winston, SST Anomalies and Surface Wind Evolution (A) MHW presence (%time, color scale, section 2.22) over 27 January –14 February 2016 from OISST, referenced to the 1993–2016 climatology. The red line marks Winston's observed track and the red star its entry onto land. Contours show the mixed-layer depth (MLD; m), highlighting a shallow layer (<15m). The white rectangle highlights the "box" region (17°S–20°S, 176°E–183°E) chosen to encompass the primary path of TC Winston as it tracked toward Fiji, as well as the broader area of elevated sea surface temperature (SST) anomalies located south, southeast and east of Fiji. The lime green markers show the position of the Argo Floats used for bias correction while the blue cross shows the position of the coastal SST data loggers (B) Time series of area-averaged SST anomalies (red) and ERA surface winds (U10 – green, V10 –dark blue). The vertical dashed magenta lines denote the MHW duration, and the vertical black line marks Winston's passage within the domain. Weak surface winds (0–2.5 m s^{-1}) during the MHW favored heat buildup and inhibited vertical mixing.

3.2.2 Surface Heat Budget and Radiative Forcing During the 2016 MHW

The MLD heat budget (Eq 1.1-1.3) was calculated to partition mixed-layer temperature tendencies into contributions from net surface heat fluxes, horizontal advection, entrainment, and residual processes, thereby identifying the mechanisms responsible for the development and maintenance of the elevated upper-ocean heat content that supported TC Winston's intensification. Anomalous

surface heat flux components (Figure 3A) show that shortwave radiation is the dominant positive contributor to the surface heat budget during the MHW development phase. Shortwave flux increases from strongly negative values (~−150 Wm^{-2}) in early January to sustained positive anomalies of ~+110–130 Wm^{-2} between ~20 January and 10 February. This period coincides with the onset and persistence of the MHW and reflects enhanced net radiative input into the upper ocean. In contrast, latent heat flux provides the primary cooling term, ranging from 0 to −50 Wm^{-2}, reflecting evaporative heat loss associated with air–sea exchange processes (Fairall et al., 1996). Longwave and sensible heat fluxes remain comparatively small (generally within ±10 Wm^{-2}) and contribute minimally to the net surface heat balance. The resulting net surface heat flux (QNet; Figure 3B) transitions from weakly negative values in early January to persistently positive values (~+50 to +120 Wm^{-2}) from mid-January through early February, with intermittent peaks exceeding +130 Wm^{-2}. This sustained positive surface forcing aligns with the period of rapid SST anomaly growth (Figure 2B) and MHW onset. During mid-February, coincident with the approach and intensification of TC Winston, QNet exhibits strong negative excursions reaching < −200 Wm^{-2}, followed by enhanced variability (approximately ±200 Wm^{-2}) through late February. These fluctuations reflect the combined effects of increased turbulent heat fluxes and reduced shortwave input associated with enhanced cloud cover and strong winds. When expressed as equivalent mixed-layer temperature tendencies (Figure 3C), shortwave heating contributes approximately +1.5 to +3.0°C day^{-1} during late January–early February, partially offset by latent heat cooling of ~−0.5 to −1.0°C day^{-1}. Longwave and sensible heat flux contributions remain small ($|\Delta T| < 0.1$ °C day^{-1}), indicating that radiative fluxes dominate the surface heat flux forcing, while turbulent fluxes act to moderate the net heat gain.

The mixed-layer heat budget (Figure 3D) shows that QNet is the dominant source of variability in the surface heat flux forcing, reaching ~+2°C day^{-1} during late January–early February and decreasing to ~−4°C day^{-1} during cyclone passage. However, the observed temperature tendency (ΔT) remains comparatively small throughout the period (typically within ±0.1°C day^{-1}), despite substantially larger variations (~6˚C) in QNet suggesting that a substantial fraction of the surface heat input was redistributed away from the mixed layer through redistributed away from the mixed layer through unresolved vertical processes such as entrainment and turbulent mixing (Large et al., 1994; Moisan & Niiler, 1998). Horizontal advection plays a secondary role, generally oscillating within ±0.5°C day^{-1}, with occasional excursions approaching ~1°C day^{-1}, suggesting limited lateral heat convergence during the event. The residual term remains small (approximately −0.5 to +0.7°C day^{-1}) but moderate compared to ΔT during the MHW period. Cumulative heat budget integrals (Figure 3E) further demonstrate that net radiative fluxes (shortwave + longwave) provide the primary source of heat input, increasing to approximately ~45–50°C (integrated equivalent hypothetical temperature) by early–mid February before stabilizing near ~35 °C equivalent. The cumulative Qnet follows a similar evolution, peaking at ~35–38 °C equivalent and stabilizing near ~20 °C, reflecting partial compensation by turbulent heat losses. The cumulative turbulent contribution (latent + sensible) decreases to approximately −20 °C equivalent. In contrast,

horizontal advection contributes minimally (within ~±5°C equivalent), reinforcing that the observed warming was predominantly driven by local surface fluxes rather than lateral heat transport. The cumulative residual remains near zero, supporting overall budget consistency. The MHW event was associated with a period of sustained positive radiative forcing and relatively weak turbulent damping, leading to significant surface heat input (Holbrook et al., 2022). However, the weak observed temperature tendency relative to the magnitude of surface forcing suggests that vertical redistribution processes play a central role in regulating mixed-layer temperature, particularly during and following cyclone-induced mixing.

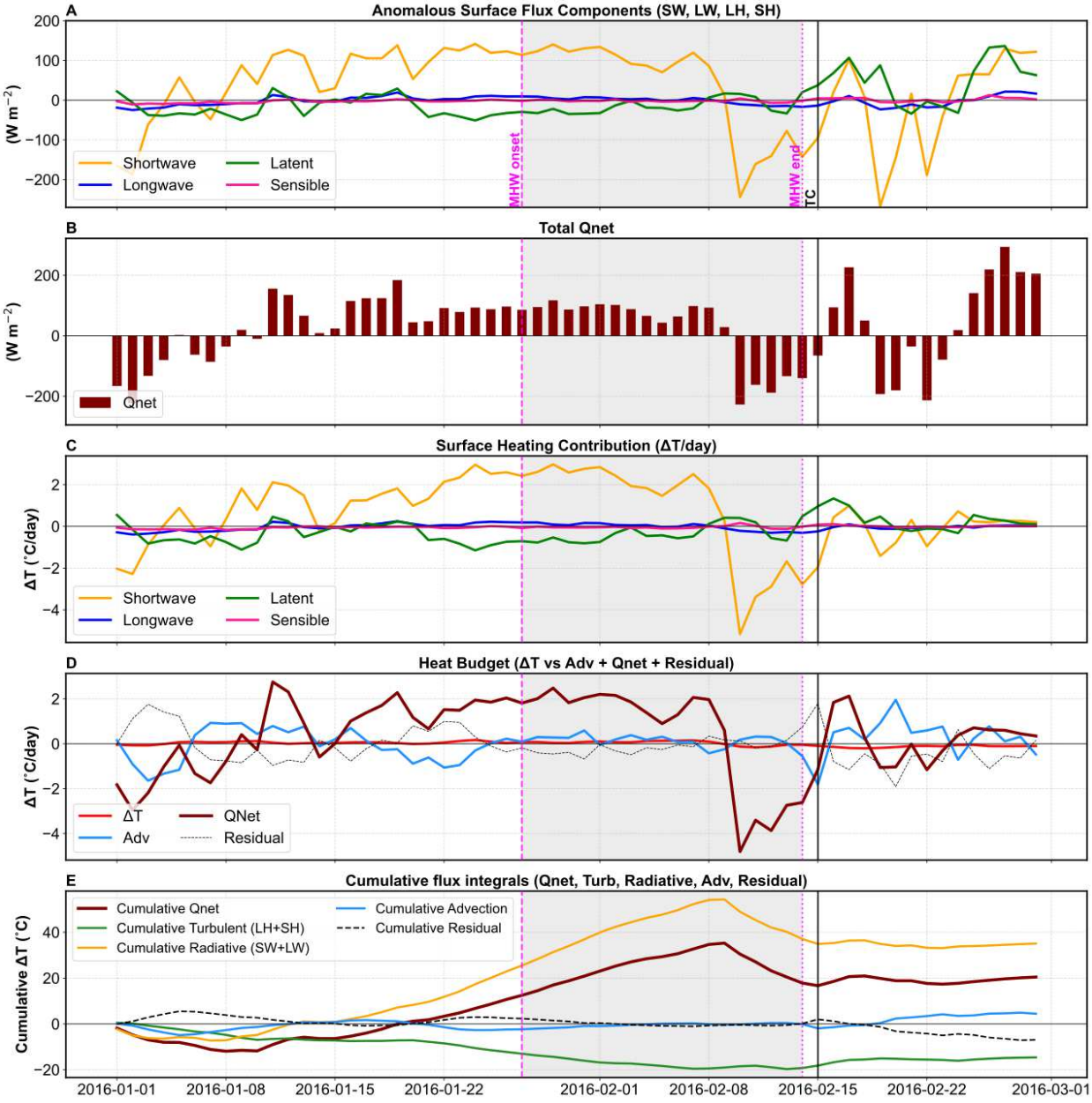


Figure 3 Surface heat budget decomposition and cumulative heating response during the 2016 MHW over the area (176–183°E, 17–20°S). (A) Anomalous surface flux components showing shortwave (SW), longwave (LW), latent (LH), and sensible (SH) heat flux anomalies. (B) Net surface heat flux (Qnet) anomalies, with positive values indicating ocean heat gain. (C) Equivalent surface heating contributions (ΔT) derived from each flux term normalized by mixed-layer heat capacity. (D) Heat

Budget illustrating observed temperature tendency (ΔT) and reconstructed terms from Qnet, horizontal advection, and residual. © Cumulative flux integrals demonstrating progressive ocean warming driven primarily by radiative input and suppressed turbulent heat loss prior to TC Winston, with cumulative QNet and radiative heating rising steadily through the MHW period (gray shading). The advection and residual terms remain small, confirming surface fluxes as the dominant source of mixed-layer preconditioning. Vertical lines mark MHW onset, end, and the TC passage. The Heat Budget confirmed that QNet, dominated by shortwave radiation, were the primary driver of the MHW.

3.2.3 Ocean Vertical Thermal Structure and MHW Evolution

The MHW is characterized by strong, surface-intensified warming confined primarily to the upper ocean, with peak anomalies exceeding +1.5°C within the upper ~20 m during late January to early February (Figure 4A). During this period, the box-averaged MLD remains shallow (~15–22m), which limits vertical mixing and promotes the retention of surface heat (Large et al., 1994). This results in a pronounced vertical temperature gradient across the base of the mixed layer. During peak MHW conditions (~8–12 February), the vertical gradient in the upper 60 m is on the order of $\Delta T/\Delta z \approx -0.04$ to -0.06°Cm^{-1}, reflecting strong near-surface stratification. Below the mixed layer, cooler anomalies of approximately −0.5 to −1.0 °C persist, enhancing the vertical temperature contrast and indicating a strongly stratified upper ocean. Although warming is surface-intensified, positive anomalies gradually extend below the mixed layer to depths of approximately 40–60m prior to cyclone passage, suggesting limited but non-negligible downward heat transfer during the MHW development phase. The persistence of a shallow MLD during this period indicates that vertical redistribution is limited relative to surface forcing, allowing heat to accumulate near the surface (e.g., Holbrook et al., 2022). Following the peak MHW and approaching the passage of TC Winston (~15 February), the upper ocean undergoes a marked transition. The mixed layer deepens to approximately 25–30 m, coincident with a reduction in near-surface temperature anomalies (to ~+0.3 °C). At the same time, positive temperature anomalies persist and become more vertically distributed below the mixed layer, particularly within the ~30–60 m depth range, indicating enhanced vertical redistribution of heat.

Vertical temperature profiles (Figure 4B) further quantify the redistribution of heat associated with the MHW and subsequent cyclone forcing. During the MHW, surface-intensified warming reaches +1.5 °C and decays rapidly with depth, with positive anomalies largely confined to the upper ~30–40 m. Following storm passage, near-surface anomalies are reduced, while slightly elevated temperatures appear below ~40 m. The difference profile (Δ; during MHW minus post-storm) highlights this vertical redistribution, with cooling of ~0.5–0.6 °C in the upper ~20 m and weaker (~0.1–0.3 °C), vertically distributed anomalies at depth, consistent with downward heat transfer driven by storm-induced mixing (Vincent et al., 2013). Depth-integrated thermal energy content was estimated from the vertical temperature anomaly profiles by integrating from the surface to 40m using endpoint values from each profile, $Q = \int_0^{40\,\mathrm{m}} \rho C_p T'(z)\, dz$. This yields average anomalous heat content of ~111 MJm^{-2} during the MHW, 53 MJm^{-2} after the storm, and 14 MJm^{-2} before the MHW. This establishes a clear ordering, $Q_{during} > Q_{after} > Q_{before}$, with heat content

increasing by ~684% from pre-MHW to peak MHW conditions, and decreasing by ~52% following storm passage. Despite this reduction, post-storm heat content remains elevated by ~275% relative to pre-MHW levels, indicating that heat removed from the mixed layer is redistributed to depth rather than lost from the upper ocean consistent with previous studies of cyclone-induced vertical heat redistribution (Vincent et al., 2013).

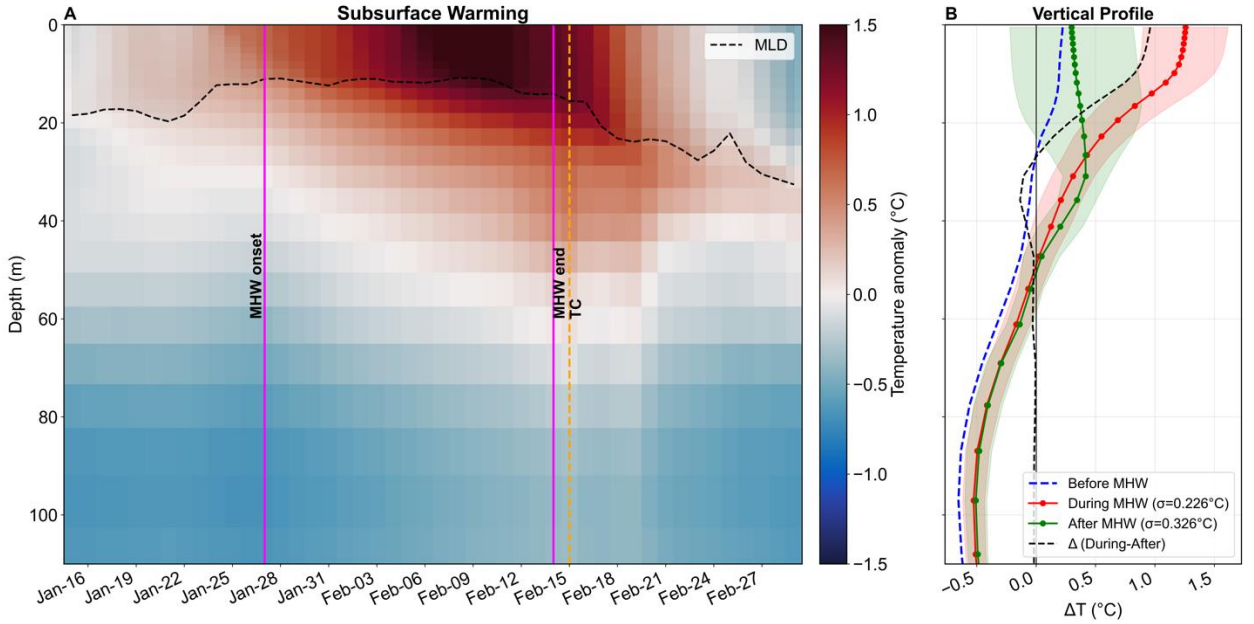


Figure 4 Ocean warming and mixed-layer evolution associated with the MHW prior to TC Winston. (A) Hovmöller section of temperature anomalies (°C) averaged over 176–183°E, 17–20°S, with MLD (black dashed line). The MHW period (between vertical magenta lines) is characterized by surface-intensified warming (> +1.5 °C) confined to the upper ~25 m. The passage of TC Winston (orange dashed line) coincides with mixed-layer deepening and a reduction in near-surface temperature anomalies. (B) Vertical temperature anomaly profiles over the same region during the MHW (red; 27 Jan–14 Feb) and after the MHW (green; 15–29 Feb), with ±1 standard deviation shading. The pre-MHW mean profile (blue dashed; 1–26 Jan) is shown for reference, and the black dashed curve denotes the difference between the MHW and post-storm mean profiles. Warming extends to ~60m during the MHW and penetrates to greater depths following the storm.

3.2.4 Brunt–Väisälä Stratification and Mixed-Layer Stability During the MHW

Upper-ocean stratification, quantified by the Brunt–Väisälä frequency (N^2), increased substantially during the MHW relative to pre-event conditions (Figure 5A). N^2 was averaged over the upper 50 m because this depth encompassed both the shallow mixed layer observed during the MHW (~13–17 m) and the upper thermocline layer extending toward the mean D26 depth (~50–60 m), where subsurface heat accumulation was observed. The metric was therefore intended to characterize the stability of the entire heat-storage layer rather than the mixed layer alone.

The largest enhancement occurred between approximately 20 and 60 m depth, where N^2 reached values approaching 3.2×10^{-4} s^{-2} during the MHW compared with approximately 2.5×10^{-4} s^{-2} before the event. Following the MHW, stratification weakened in the upper 20–30 m but exhibited a deeper maximum near 40 m depth, reaching approximately 4.3×10^{-4} s^{-2}. Across all phases, the thermal component dominated the stratification signal, while the haline contribution remained

comparatively small (Figure 5A). A clear inverse relationship is observed between mixed-layer stratification and mixed-layer depth (MLD) (Figure 5B). Daily values show that periods of stronger stratification were generally associated with shallower mixed layers, yielding a correlation coefficient of $r = -0.65$ ($\rho = -0.85$; $r^2 = 0.43$). The shallowest mixed layers occurred during intervals of elevated N^2, whereas deeper mixed layers were associated with weaker stratification.

Boxplot statistics further demonstrate the strengthening of upper-ocean stability during the MHW (Figure 5C). Median mixed-layer N^2 increased by approximately 68% from pre-MHW to MHW conditions. Following the event, median stratification decreased by approximately 88% relative to MHW values. The MHW period also exhibited a narrower interquartile range than the post-event phase, indicating more persistent and less variable stratification during the event. Figure 5 suggests that the MHW was characterized by enhanced thermally driven stratification and a shallower mixed-layer structure prior to TC Winston.

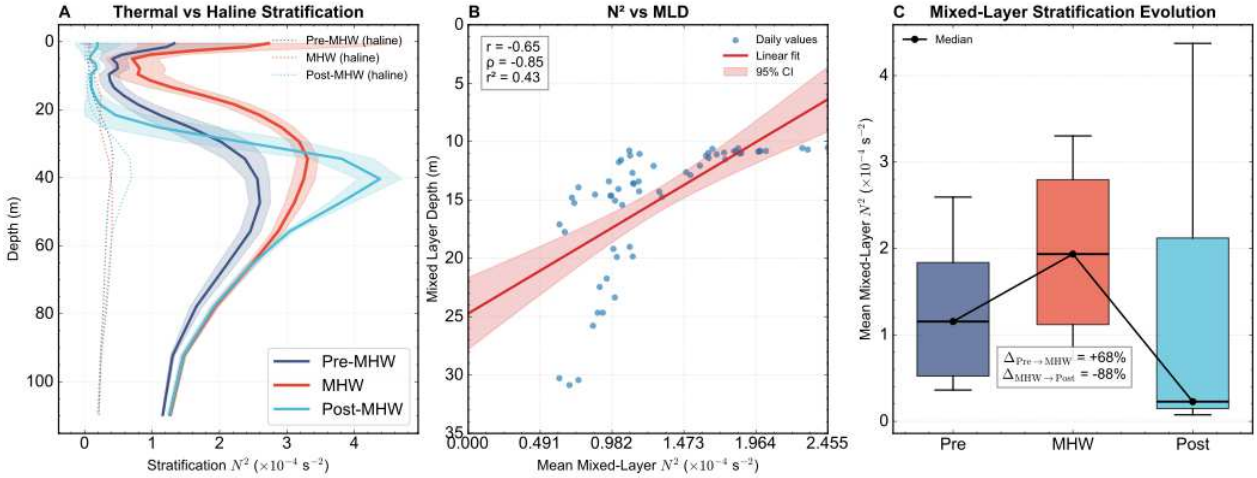


Figure 5 Stratification during the MHW event. Brunt–Väisälä frequency squared (N^2) averaged over the "box" region (Figure 2). (A) Vertical profiles for pre-MHW, MHW, and post-MHW periods. Solid lines denote thermal stratification and dotted lines indicate the haline component; shading represents variability. (B) MLD (m) as a function of stratification in the top 50 m. Points show daily values; the solid line is the linear regression with 95% confidence interval (shading). Correlation statistics are $r = -0.65$, $\rho = -0.85$, and $r^2 = 0.43$. (*C*) Boxplots of stratification for pre-MHW, MHW, and post-MHW periods. Black markers indicate medians (~1.2, ~1.9, and 0.2 $\times 10^{-4}$ s^{-2}), with percentage changes of +68% and −88%.

3.2.5 Ocean Heat Storage

The previous section showed that the 2016 MHW modified the upper-ocean structure through enhanced stratification and persistent mixed-layer shoaling. Because the mixed layer is the layer directly altered by surface warming, we first quantify the resulting anomalous heat storage within the mixed layer using mixed-layer ocean heat content (OHC'_{MLD}). We then examine whether this anomalous heat remained confined to the mixed layer or extended into the subsurface ocean by evaluating heat content integrated to 100 m (OHC'_{100}) and to the 26°C isotherm (OHC'_{D26}; Eq.2; TCHP). Finally, we assess the persistence of the accumulated heat reservoir using the equivalent

cooling timescale ((t_{eq})), which provides a measure of how long the stored heat could be sustained against observed turbulent heat loss.

The thermal anomaly was not restricted to the mixed layer. Both OHC′100 and OHC′D26 increased more rapidly and attained substantially larger magnitudes than OHC′MLD (Figure 6A). OHC′100 increased from negative anomalies in late January to approximately 150 MJ m^{-2} by mid-February, while OHC′D26 reached approximately 170 MJ m^{-2}. The larger anomalies in OHC'_{100} and OHC'_{D26} relative to OHC'_{MLD} indicate that a substantial fraction of the MHW-induced heat anomaly was stored beneath the mixed layer and extended into the upper thermocline. Because OHC'_{D26} integrates heat content to the 26°C isotherm whereas OHC'_{MLD} is limited to the mixed layer, the separation between the two metrics reflects the accumulation of anomalous heat within the upper thermocline beneath the mixed layer.

The persistence of the accumulated heat reservoir is illustrated by the equivalent cooling timescale, teq (Figure 6B). Prior to MHW onset, t_{eq} remained below approximately 2 days, indicating limited resistance to turbulent heat loss. As OHC'_{100} and OHC'_{D26} increased, t_{eq} rose steadily, exceeding 3 days by late January and reaching approximately 8-10 days near the mature phase of the MHW. This increase occurred despite continued positive turbulent heat fluxes from the ocean to the atmosphere (~150–250 Wm^{-2}), indicating that the accumulated heat reservoir was sufficiently large to sustain prolonged atmospheric cooling. Following TC Winston, both OHC anomalies and t_{eq} declined rapidly.Click or tap here to enter text.

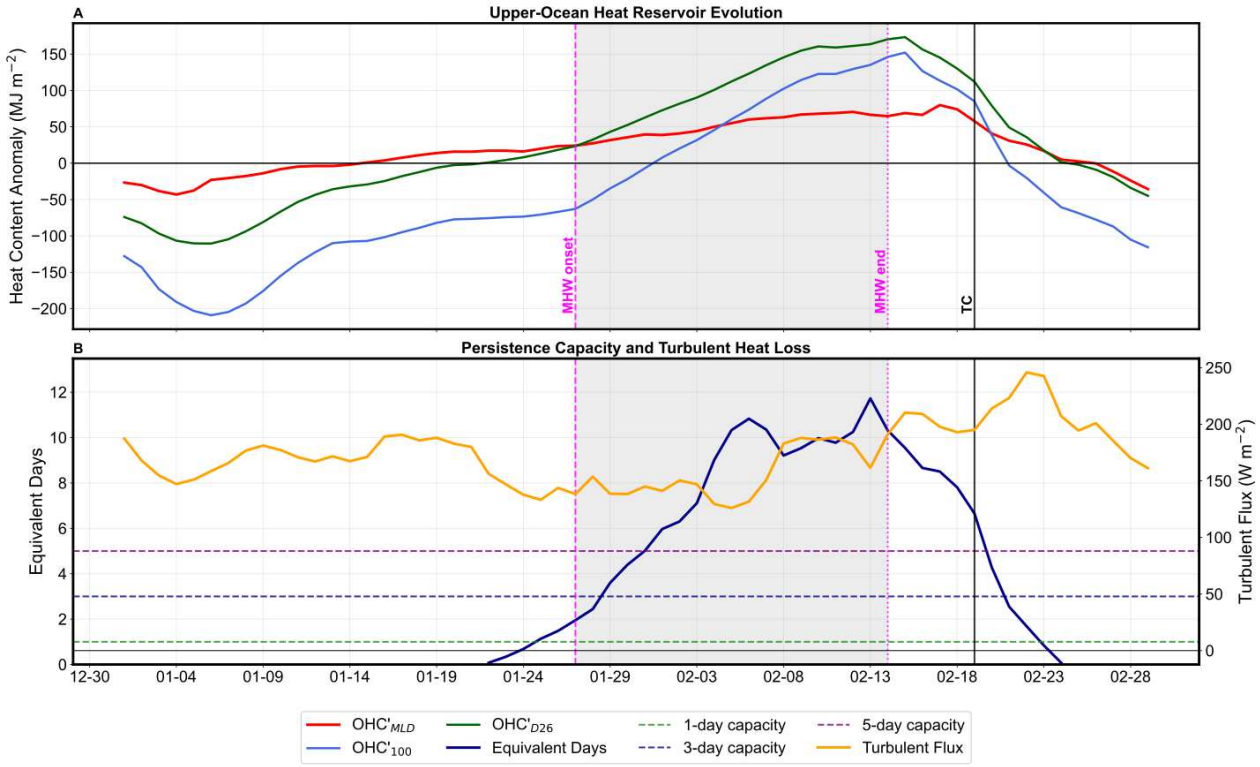


Figure 6 Evolution of upper-ocean heat storage and persistence during the January–February 2016 MHW preceding TC Winston. (A) Anomalous OHC relative to 1993-2016 baseline integrated over the mixed layer (OHC'_{MLD}, upper 100 m (OHC'_{100}), and to the 26°C isotherm (OHC'_{D26}). Differences between OHC'_{MLD} and OHC'_{D26} indicate anomalous heat storage beneath the mixed layer within the upper thermocline. (B)Equivalent cooling timescale (t_{eq}; blue), representing the persistence of the accumulated heat reservoir under the observed turbulent heat flux (orange). Horizontal dashed lines denote 1-, 3-, and 5-day persistence thresholds. Vertical magenta lines indicate MHW onset and termination, and the black vertical line marks the passage of Tropical Cyclone Winston. Positive turbulent heat flux denotes ocean-to-atmosphere heat transfer.

During the mature MHW phase, net surface heat flux initially drives warming (Figure 3C), but elevated stratification subsequently confine this heat within the shallow mixed layer (Balaguru et al., 2015) (Figures 4–5). Despite continued ocean heat loss from upward turbulent heat flux (Figure 6B), OHC continues to increase and persist within and below the MLD (Figure 6).

3.3 Upper-Ocean Heat Reservoir Evolution During Rapid Intensification

Section 3.2 demonstrated that the MHW established a persistent upper-ocean heat reservoir extending beneath the mixed layer (Figure 4). We now examine how this thermal structure evolved during TC Winston's rapid intensification through analyses of upper-ocean thermal structure, heat-content depletion, and ocean–atmosphere energy exchange.

3.3.1 Along-Track Upper-Ocean Thermal Response and Heat Reservoir Evolution

The along-track thermal structure revealed substantial upper-ocean modification during the period surrounding TC Winston's rapid intensification and peak intensity (Figure 7). Pre-cyclone

temperatures exceeded 29°C within the upper ocean, while positive temperature differences ($\Delta T = T_{before} - T_{after}$) indicated widespread cyclone-related cooling. Cooling commonly exceeded 0.5–1.5°C, locally surpassed 2°C, and extended from the surface to depths of approximately 200–250 m (Figure 7A). The strongest cooling occurred between 16 and 20 February and exhibited considerable vertical variability, with both surface-intensified and subsurface cooling structures evident along the storm track. The corresponding depth-resolved heat-content anomalies (ΔOHC) were predominantly positive during the rapid-intensification period, indicating lower heat content in the post-cyclone state relative to the pre-cyclone state (Figure 7B). Positive anomalies were distributed throughout much of the water column but were most pronounced between approximately 300 and 600 m depth during 16–19 February, where values exceeded 150 MJ m^{-2}. These elevated anomalies persisted through RI-2 and RI-3 (Figure 7 CD). before weakening after peak intensity. Additional positive anomalies were also evident following cyclone passage around 21–23 February.

The evolution of upper-ocean thermal structure revealed a pronounced depth-dependent response during the rapid intensification of TC Winston (Figure 7 C). Prior to RI, D20 and D26 remained relatively deep, consistent with the pre-existing MHW state. Beginning around 14 February, D20 and D26 isotherms shoaled progressively, with the magnitude of shoaling increasing with depth. D26 shoaled by approximately 50–70 m, whereas D20 shoaled by nearly 200 m and reached its maximum displacement during RI-2. In contrast, mixed-layer depth varied by only ~20 m throughout the event. Following peak intensity, D20 and D26 rapidly relaxed toward their pre-storm positions, while the mixed layer evolved more gradually. The integrated heat reservoirs exhibited a similar evolution (Figure 7D). Positive heat-content anomalies emerged near the onset of RI and strengthened through RI-1 and RI-2, with the response increasing systematically with reservoir depth. H100 reached approximately 2000 MJ m^{-2}, while H300 and H600 increased to roughly 7000 and 8000 MJ m^{-2}, respectively. TCHP followed the same temporal pattern but with substantially smaller amplitudes (~800–1000 MJ m^{-2}). All reservoirs underwent a rapid reversal following peak intensity, with the strongest pre-peak buildup and post-peak decline occurring in H300 and H600.

Fractional depletion analysis further highlights differences among the heat reservoirs during rapid intensification (Figure 8). During RI-1, depletion was modest in HML, H100, and H300 and was nearly absent in H600, whereas TCHP exhibited substantially larger depletion than all other reservoirs. During RI-2, depletion increased across H100, H300, and H600, with H300 exhibiting the largest fractional reduction among the integrated heat-content reservoirs. By RI-3, H100, H300, and H600 continued to exhibit positive depletion of similar magnitude, while HML underwent a sign reversal and became strongly negative relative to its RI reference state. Throughout all three rapid-intensification phases, TCHP exhibited the largest fractional depletion, increasing from approximately 80% during RI-1 to near-complete depletion by RI-3.

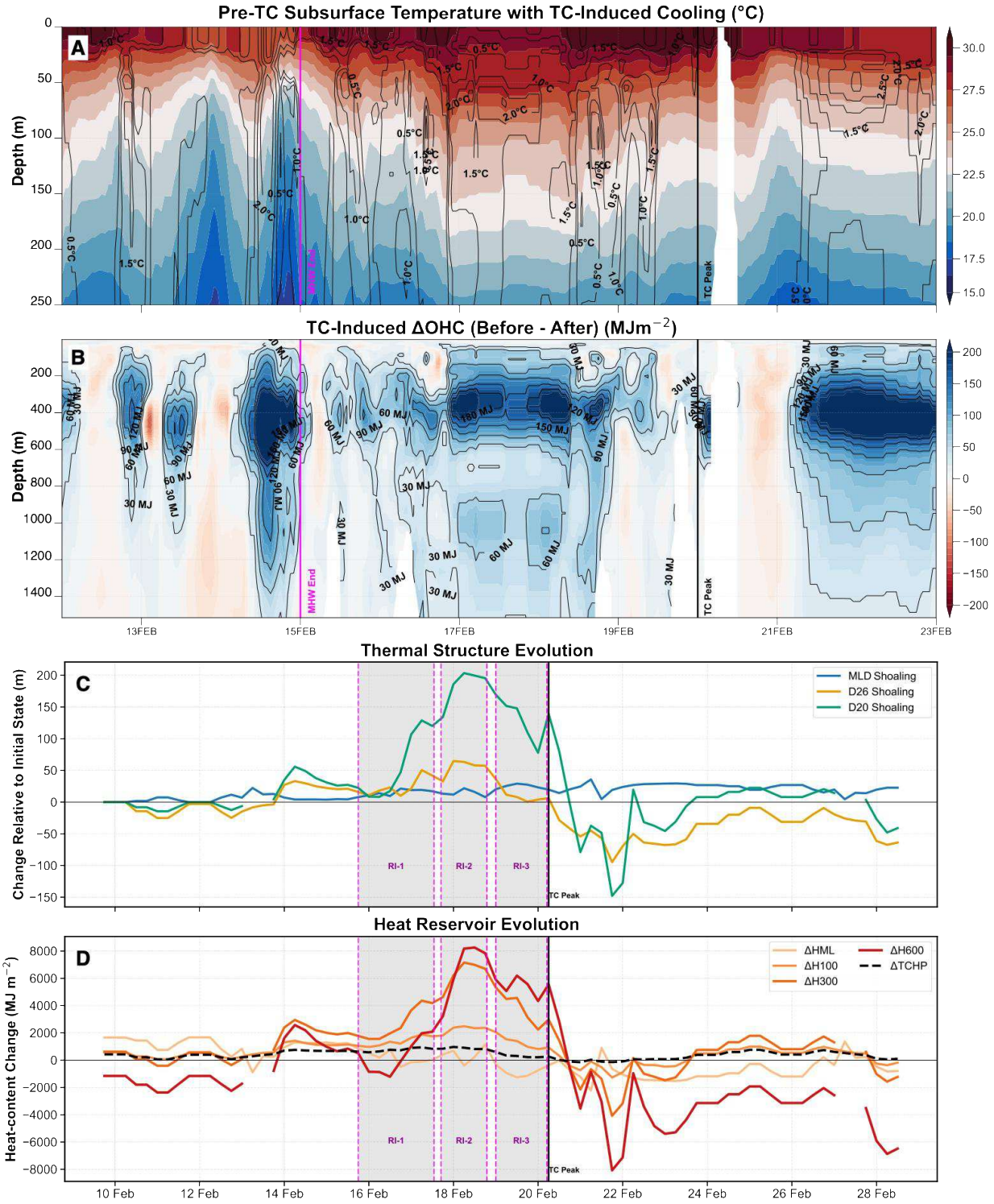


Figure 7 Along-track evolution of ocean temperature and heat reservoirs of TC Winston. Vertical profiles are sampled along the storm track at fixed temporal offsets of −7 days (pre-TC) and +7 days (post-TC) relative to each position on the TC track. (A) Shading shows pre-TC temperature (°C) as a function of time and depth (m). Overlaid black contours denote TC-induced cooling magnitude, defined as positive values of $\Delta T = T_{before} - T_{after}$, contoured at 1°C intervals. (B) Shading shows depth-resolved ocean heat content change (MJm^{-2}), computed as $\Delta OHC_{(z,t)} = \rho C_p (T_{before} - T_{after}) \Delta z$, where ρ =1025 kgm^{-3} and C_p=3850 Jkg^{-1}°C^{-1}. Black contours indicate positive OHC anomalies (heat loss) at discrete levels (MJm^{-2}). Time corresponds to storm track progression. (C) Changes in mixed-layer depth (MLD), depth of the 26°C isotherm (D26), and depth of the 20°C isotherm (D20)

relative to peak conditions. Positive values indicate mixed-layer deepening and thermocline shoaling relative to the peak-intensity state. (D) Evolution of mixed-layer heat content (HML), heat content integrated to 100 m (H100), 300 m (H300), and 600 m (H600), together with TCHP. Grey shaded regions denote the three rapid-intensification (RI) phases, bounded by magenta dashed lines, while the vertical black line marks the time of peak cyclone intensity and landfall.

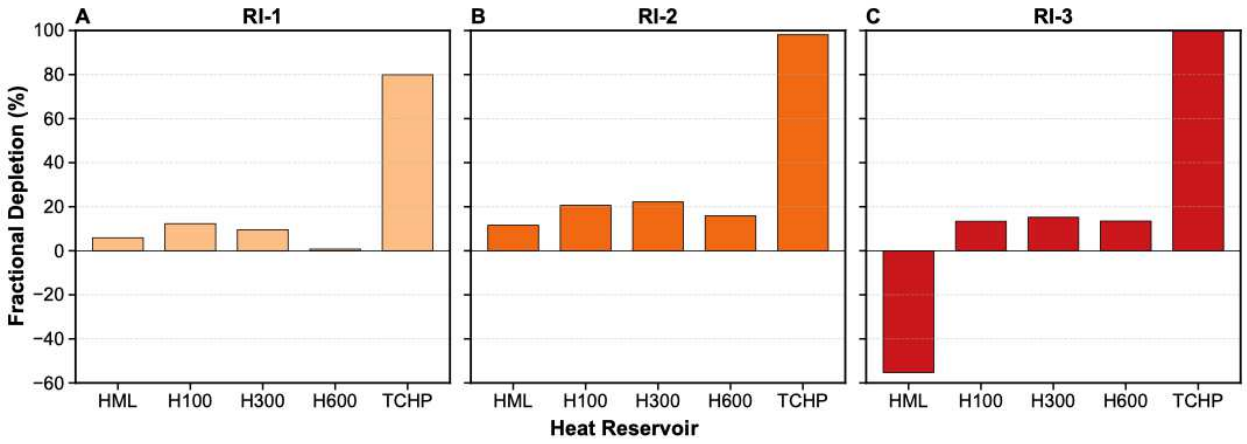


Figure 8 Fractional depletion of mean upper-ocean heat reservoirs during the three rapid intensification phases of TC Winston. Vertical profiles are sampled along the storm track at fixed temporal offsets of −7 days (pre-TC) and +7 days (post-TC) relative to each position on the TC track. Bars show the mean percentage reduction in mixed-layer heat content (HML), heat content integrated to 100 m (H100), 300 m (H300), and 600 m (H600), and tropical cyclone heat potential (TCHP), relative to their pre-RI values.

3.3.2 Along Track Energetic Evolution and Temporal Sequencing During Rapid Intensification

This transition from stored to dynamically accessible heat is resolved in the coupled energy diagnostics (Figure 10), which quantify the temporal sequencing between upper-ocean heat extraction, turbulent flux response, and atmospheric kinetic energy growth. To examine the evolution of air–sea energy exchange during rapid intensification in TC Winston, we analyse RI phase-averaged diagnostics of TCHP, atmospheric kinetic energy (KE), and turbulent surface heat flux ($Q_{turβ}$), together with their temporal tendencies (Table 1; Figure 10). Although several heat-content metrics are examined in Section 3.3.1, the analysis presented here focuses on tropical cyclone heat potential (TCHP; Eq. 2). During RI, mixed-layer heat content (HML) exhibited a net increase relative to its pre-storm state, whereas TCHP underwent progressive depletion. This contrasting behaviour indicates that the energetically important oceanic changes associated with RI were concentrated beneath the mixed layer, making TCHP a more appropriate metric for examining the coupling between ocean heat extraction, surface enthalpy fluxes, and atmospheric energy growth.

Temporal tendencies were calculated using centered finite differences and evaluated across a pre-RI phase, three RI sub-phases (RI-1, RI-2, and RI-3), and a post-RI phase. Prior to RI, Winston was located over comparatively modest OHC conditions ($206 MJm^{-2}$) and experienced strong vertical wind shear ($17.2 ms^{-1}$. Storm KE averaged $981 Jkg^{-1}$, while the mean KE tendency was

slightly negative ($-3.3 Jkg^{-1}h^{-1}$), indicating little net intensification. During this phase, ocean-to-atmosphere heat transfer was already substantial, with mean heat-loss rates of approximately $211 Wm^{-2}$, suggesting that although energy was being transferred from the ocean surface, the strongly sheared environment limited its conversion into cyclone intensification.

The onset of RI coincided with a marked improvement in environmental conditions. During RI-1, TCHP approximately doubled to $415 MJm^{-2}$ while vertical wind shear decreased to $5.7 ms^{-1}$. Although mean storm KE remained relatively modest ($625 Jkg^{-1}$), the KE tendency became positive ($+8.0 Jkg^{-1}h^{-1}$), signalling the transition into a strengthening phase. Mean heat-loss rates remained near $93 Wm^{-2}$, consistent with continued ocean-to-atmosphere energy transfer under substantially more favourable atmospheric conditions. RI-2 was characterised by the highest OHC of the event ($769 MJm^{-2}$) and the slowest translation speed ($2.7 ms^{-1}$), indicating prolonged residence over a deep upper-ocean heat reservoir. Vertical wind shear remained weak ($7.3 ms^{-1}$), while mean storm KE increased to $1327 Jkg^{-1}$ and maintained positive growth rates ($+7.6 Jkg^{-1}h^{-1}$). Together, these conditions represent the most favourable thermodynamic environment encountered during the intensification period. The most energetic stage of the cyclone occurred during RI-3. Although mean OHC decreased slightly relative to RI-2, it remained elevated ($705 MJm^{-2}$), while vertical wind shear reached its lowest phase-mean value ($4.8 ms^{-1}$). Mean storm KE increased substantially to $2295 Jkg^{-1}$, and the KE tendency reached its maximum ($+25.8 Jkg^{-1}h^{-1}$). Heat-loss rates also increased to $178 Wm^{-2}$. The time series reveals a pronounced burst of KE growth during RI-3, coincident with strong short-term fluctuations in both OHC and turbulent heat-flux tendencies (Figure 10A–C). These results suggest that intensification occurred through episodic bursts of energy conversion rather than a steady, continuous transfer process.

Following RI, storm KE remained elevated ($1741 Jkg^{-1}$), but the mean KE tendency became strongly negative ($-17.2 Jkg^{-1}h^{-1}$), indicating weakening. At the same time, vertical wind shear increased rapidly to $16.5 ms^{-1}$, approaching pre-RI values. Despite the largest mean heat-loss rates of the event ($377 Wm^{-2}$), the increasingly hostile atmospheric environment limited further intensification, highlighting the dominant role of atmospheric forcing during the decay phase. The temporal evolution shown in Figure 8 supports this interpretation. Positive KE tendencies become progressively larger through the RI period and peak during RI-3 (Figure 10A), while TCHP and turbulent heat-flux tendencies exhibit substantial short-term variability (Figures 10B–C). The environmental evolution panel (Figure 10D) indicates that TC Winston's rapid intensification occurred during a period when OHC coincided with a marked reduction in environmental VWS. The phase composites (Figure 10E) show that RI phases were associated with above-average TCHP, relatively weak VWS, and elevated cyclone kinetic energy. Elevated TCHP likely helped sustain air–sea enthalpy fluxes by reducing cyclone-induced cooling of the upper ocean (Jaimes et al., 2015; Lin et al., 2009a; Price, 1980), while weak vertical wind shear favoured the maintenance of a vertically aligned vortex and persistent deep convection(DeMaria, 1996). The concurrence of

these conditions is consistent with established rapid-intensification theory, whereby favourable oceanic and atmospheric environments support enhanced storm strengthening (Lin et al., 2009b).

Phase	Mean THCP MJ/m^2	Mean dOHC/dt W/m^2	Mean Storm KE J/Kg	Mean dKE/dt J/Kg/h	Mean Qturb W/m^2	Mean dQturb W/m^2h	Mean VWS m/s	Mean tSpeed m/s
Pre-RI	205	790	980	-3.3	210	2.55	17	6.3
RI-1	415	-3030	624	8.0	93.2	-0.62	5.7	4.9
RI-2	769	519	1327	7.6	98.9	0.21	7.5	2.4
RI-3	704	-198	2295	25.8	178.1	-3.12	4.8	6.5
Post-RI	377	912	174	-17.2	377.1	-0.03	16.5	3.9

Table 1 Along-track diagnostic synthesis of coupled ocean–atmosphere conditions across TC Winston's path. RI-averaged ocean–atmosphere energy diagnostics for TC Winston, OHC, referenced to the 26 °C isotherm, atmospheric kinetic energy (KE), turbulent surface heat flux ($Q_{turβ}$), and their temporal tendencies, along with vertical wind shear (VWS) and storm translation speed (tSpeed). Values are computed for the pre-RI, three rapid intensification sub-phases (RI-1 to RI-3), and post-RI periods. Tendencies are calculated using centered finite differences at ~2 h resolution. Positive dOHC/dt denotes a decrease in upper-ocean heat content, while negative $Q_{turβ}$ indicates upward turbulent heat flux from the ocean to the atmosphere.

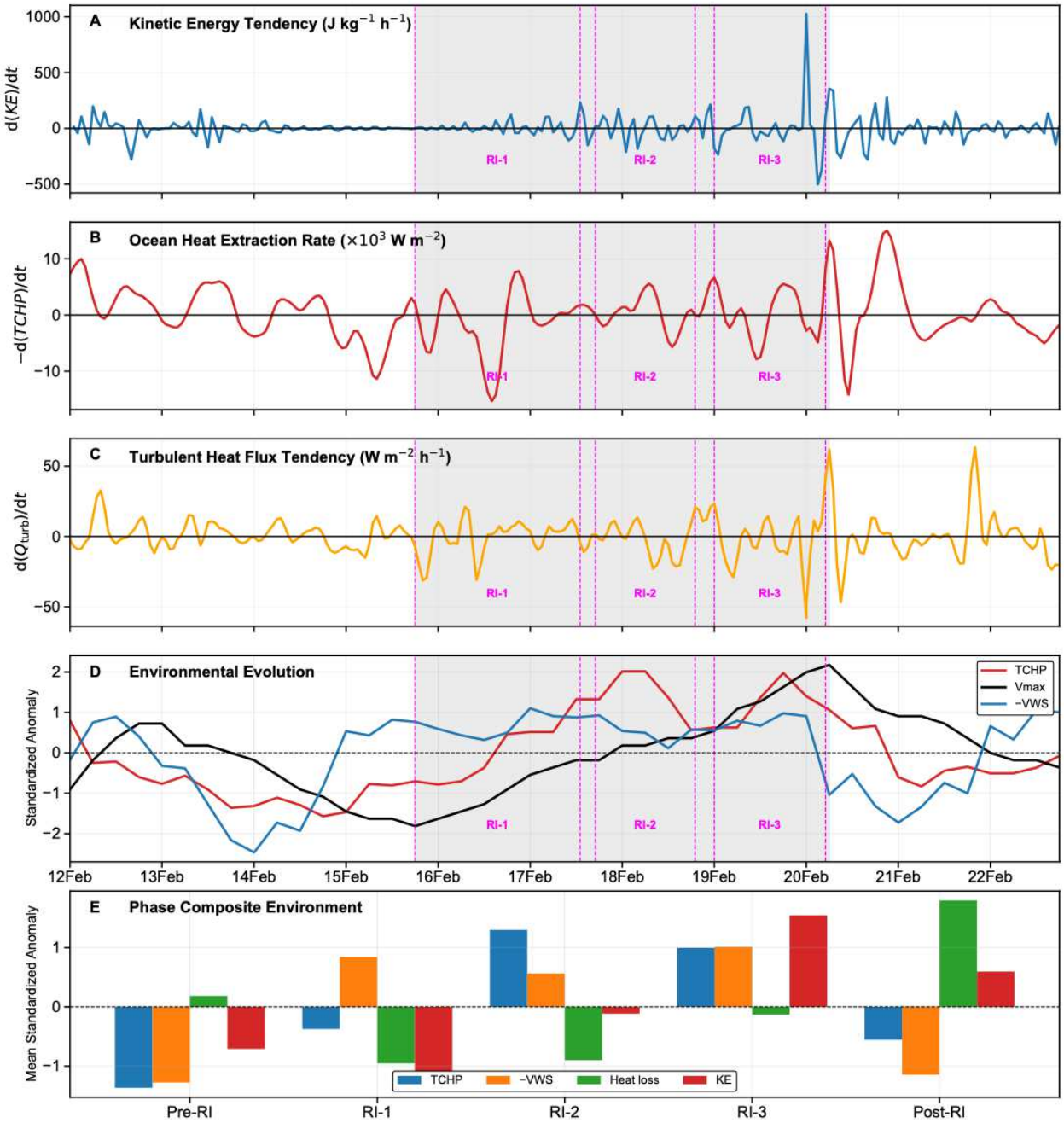


Figure 10 Evolution of oceanic and atmospheric energy diagnostics during the rapid intensification (RI) lifecycle of Tropical Cyclone Winston. (A) Environmental kinetic energy tendency (dKE/dt; J kg^{-1} h^{-1}). Positive values indicate increasing atmospheric kinetic energy available to the storm environment. (B) Ocean heat extraction rate, expressed as −d(TCHP)/dt (×10^3 W m^{-2}), where TCHP is the ocean heat content above the 26°C isotherm. Positive values indicate depletion of the upper-ocean heat reservoir (ocean heat loss), while negative values indicate replenishment or increasing OHC. (C) Tendency of turbulent surface heat flux (dQ_turb/dt; W m^{-2} h^{-1}). Vertical dashed lines denote the three RI phases identified from the storm intensity record. (D) Standardized anomalies of TCHP, maximum sustained wind speed (Vmax), and vertical wind shear (VWS). Positive OHC anomalies indicate an enhanced subsurface heat reservoir, while positive VWS anomalies indicate stronger environmental shear. (E) Phase-composite standardized anomalies of TCHP, −VWS, turbulent heat loss (−Q_turb), and kinetic energy (KE). Positive values therefore represent enhanced ocean heat availability, weaker vertical wind shear, greater ocean-to-atmosphere heat transfer, and larger atmospheric kinetic energy, respectively.

4. Discussion

Our results demonstrate that the rapid intensification of TC Winston emerged from a preconditioned upper-ocean state established by the 2016 MHW. Enhanced radiative forcing, weak winds, and strong upper-ocean stratification produced a shallow mixed layer and promoted the accumulation of heat within and immediately beneath the mixed layer (Large et al., 1994; Moisan & Niiler, 1998), generating a vertically structured upper-ocean heat reservoir. Mixed-layer heat budget diagnostics indicate that a substantial fraction of the surface heat input was redistributed below the mixed layer rather than retained locally, leading to the development of anomalously warm upper-thermocline waters prior to cyclone passage. The rapid intensification of Winston was associated with the subsequent mobilization of this stored heat through storm-induced mixing and air–sea energy exchange. Rather than being confined to the mixed layer, the strongest heat-content depletion occurred within subsurface reservoirs, demonstrating that the energetically important oceanic response extended well below the pre-storm mixed-layer depth. Rapid intensification therefore depended not only on the magnitude of upper-ocean heat storage, but also on its vertical distribution and accessibility under favourable atmospheric conditions.

4.1 MHW Preconditioning and Formation of a Vertically Structured Heat Reservoir

The February 2016 marine heatwave established a highly favourable upper-ocean environment prior to the rapid intensification of TC Winston. MHW conditions were nearly continuous (>90% occurrence) across the region where Winston subsequently intensified, and the cyclone track passed directly through the core of the warm anomaly. During this period, weak surface winds (<5 m s^{-1}) coincided with exceptionally shallow mixed layers (~13–17m), while SST anomalies increased from approximately −0.5°C to more than +2°C. Together, these conditions indicate that surface heat accumulated within a weakly mixed upper ocean, establishing the thermodynamic preconditioning state encountered by the cyclone. The mixed-layer heat budget demonstrates that this preconditioning involved more than surface warming. Enhanced shortwave radiation was the dominant source of heat gain, producing sustained positive net surface heat fluxes that frequently exceeded +50–120 W m^{-2} and equivalent mixed-layer heating rates approaching +2°C day^{-1}. However, observed mixed-layer temperature tendencies remained comparatively small, generally within ±0.1°C day^{-1}. Because both horizontal advection and residual heat-budget terms were small, the absorbed surface heat cannot be explained solely by warming of the mixed layer. Instead, the results indicate that a substantial fraction of the accumulated heat was redistributed beneath the mixed layer rather than retained locally (Large et al., 1994; Moisan & Niiler, 1998). The reduction in net surface heat fluxes (~6˚C; Figure 3A-D) during early February was primarily driven by a sharp decline in shortwave radiation, Dutheil et al. (2024), linked the termination of the 2016 Southwest Pacific MHW to a shift from suppressed to convective MJO phases, resulting in increased cloud cover and reduced solar heating prior to the strongest impacts of TC Winston.

The vertical thermal structure provides direct evidence for this redistribution. During the mature MHW, warming exceeded +1.5°C within the upper 20m and progressively extended below the mixed layer to depths of approximately 40–60m prior to Winston's arrival. Concurrently, estimated

upper-ocean heat content increased from approximately 14 MJm^{-2} before the MHW to approximately 111 MJm^{-2} during its mature phase. Although heat content decreased following cyclone passage, post-storm values remained substantially elevated (~53 MJm^{-2}), indicating that a large fraction of the accumulated thermal anomaly persisted within the upper ocean. The MHW may have generated a vertically extended heat reservoir rather than a surface-confined warm anomaly. Enhanced stratification appears to have been central to the development of this structure. Brunt–Väisälä frequency increased substantially during the MHW, with median values approximately 68% greater than before the event, favouring the accumulation and retention of anomalous heat within and immediately beneath the mixed layer (Balaguru et al., 2012; de Boyer Montégut et al., 2004). The strongest evidence for subsurface heat storage is provided by the heat-content diagnostics. Heat-content anomalies integrated to 100m (OHC′100) and to the 26°C isotherm (OHC′D26) reached approximately 150 and 170 MJm^{-2}, respectively, substantially exceeding anomalies confined to the mixed layer. These results demonstrate that heat accumulation during the MHW was not restricted to the surface layer but extended into the upper thermocline. Moreover, the equivalent cooling timescale increased from less than two days before the MHW to approximately 8–10 days during its mature phase, indicating that the accumulated thermal anomaly became increasingly resistant to removal by atmospheric cooling. The objective of the 2016 MHW was not simply elevated SST, but the formation of a persistent, vertically structured upper-ocean heat reservoir. Sustained radiative forcing, weak winds, mixed-layer shoaling, and enhanced stratification produced an upper ocean in which anomalous heat accumulated both within and beneath the mixed layer and remained stored for timescales substantially longer than typical atmospheric cooling would suggest. This preconditioned thermal structure provided the oceanic energy reservoir that was later available for interaction with TC Winston during rapid intensification.

4.2 Storm-Induced Access to the Subsurface Heat Reservoir During Rapid Intensification

The vertically structured heat reservoir established during the MHW strongly influenced the upper-ocean response during the rapid intensification of TC Winston. The evidence of this response was that the largest cyclone-induced thermal changes occurred beneath the pre-storm mixed layer, indicating that the oceanic response extended well beyond the shallow surface layer established during the heatwave. Along-track temperature and heat-content diagnostics show that cyclone-induced cooling penetrated to depths of approximately 200–250m and was not confined to the upper mixed layer. Positive ΔOHC anomalies, representing heat loss from the pre-storm ocean state, were distributed throughout much of the water column but were most pronounced between approximately 300 and 600m depth during the rapid-intensification period (Han et al., 2025; greater 1000m). The strongest heat-content changes occurred within subsurface reservoirs rather than at the surface. The evolution of upper-ocean structure further supports this interpretation. During rapid intensification, both the 20°C and 26°C isotherms shoaled substantially, with D20 exhibiting considerably larger displacements than D26, while mixed-layer depth varied comparatively little. Concurrently, heat-content anomalies increased with reservoir depth, with the

largest pre-peak buildup and subsequent post-peak decline occurring in H300 and H600. Fractional depletion diagnostics reveal that heat extraction progressively penetrated deeper into the water column through successive rapid-intensification phases. During RI-1, depletion was concentrated within the upper ocean and was weak below 600 m. By RI-2 and RI-3, depletion extended into progressively deeper reservoirs, with H300 and H600 exhibiting larger fractional losses than earlier in the intensification cycle. In contrast, TCHP experienced substantial depletion throughout all rapid-intensification phases and approached near-complete depletion by RI-3. The warm thermocline reservoir beneath the mixed layer was heavily utilised during rapid intensification (Jaimes & Shay, 2015; Shay et al., 1999). While H100, H300, H600, and TCHP continued to exhibit net depletion during the later stages of rapid intensification, HML underwent a sign reversal and increased relative to its earlier rapid-intensification state. This divergence suggests that the mixed layer and subsurface reservoirs were dynamically coupled during storm intensification. The simultaneous increase in HML and depletion of the deeper heat reservoirs suggests vertical redistribution of heat within the upper ocean during rapid intensification. This is consistent with the enhanced entrainment and vertical mixing known to accompany tropical cyclone forcing, whereby heat stored beneath the mixed layer can be incorporated into the deepening surface layer while deeper reservoirs are progressively depleted (Jaimes & Shay, 2015; Shay et al., 1999).

The diagnostics of intensification suggests that this heat extraction occurred while conditions remained favourable for storm intensification. Elevated OHC anomalies, increasing atmospheric kinetic energy, enhanced turbulent heat loss (Emanuel, 1999; Shay et al., 1999), and weak vertical wind shear coexisted throughout much of the rapid-intensification period. The timing of these responses indicates that the subsurface heat reservoir established during the MHW remained dynamically relevant as Winston intensified. The contribution of the MHW extended beyond elevated sea-surface temperatures. The MHW produced a vertically distributed upper-ocean heat reservoir that was subsequently accessed during rapid intensification, with the strongest thermal adjustments and heat-content depletion occurring below the mixed layer. Ocean heat availability during rapid intensification therefore depended not only on the magnitude of stored heat but also on its vertical distribution within the upper ocean.

4.3 Coupled Ocean–Atmosphere Energy Exchange During Rapid Intensification

Rapid intensification occurred during a period of strong coupling between the preconditioned upper ocean and the atmosphere. The subsurface heat reservoir established during the MHW was actively depleted throughout the rapid-intensification period, while turbulent heat transfer from the ocean to the atmosphere and atmospheric kinetic energy increased simultaneously. The temporal alignment of these tendency signals indicates that ocean heat extraction, air–sea energy exchange, and atmospheric energization evolved together during intensification rather than as independent processes. Along-track diagnostics show that rapid intensification coincided with elevated ocean heat availability and progressive depletion of subsurface heat reservoirs. The strongest heat-content reductions occurred below the mixed layer, particularly within the deeper

heat reservoirs and the warm thermocline reservoir represented by TCHP. At the same time, turbulent heat loss from the ocean remained elevated, indicating sustained transfer of energy from the ocean to the atmosphere throughout the intensification period. Fractional depletion diagnostics further demonstrate that heat extraction progressively penetrated deeper into the water column through successive RI phases, with TCHP approaching near-complete depletion by RI-3. The atmospheric environment further enhanced the efficiency of this coupled response. Rapid intensification occurred under relatively weak vertical wind shear (Frank & Ritchie, 2001), while atmospheric kinetic energy increased steadily and reached its largest values during the later stages of RI. Environment-composite diagnostics show that elevated OHC, enhanced turbulent heat transfer, increasing kinetic energy, and weak shear coexisted throughout the rapid-intensification period. The simultaneous occurrence of these favourable oceanic and atmospheric conditions (Park et al., 2012) suggests that neither the ocean nor the atmosphere alone controlled the intensification process.

Winston's rapid intensification therefore emerged from the interaction between a pre-existing subsurface heat reservoir and a favourable atmospheric environment. The MHW increased both the magnitude and vertical extent of upper-ocean heat storage, while the cyclone progressively accessed and depleted this reservoir during intensification. The temporal alignment of ocean heat extraction, enhanced turbulent heat transfer, increasing atmospheric kinetic energy, and weak vertical wind shear indicates a coupled ocean–atmosphere energetic response in which the availability of subsurface heat and favourable atmospheric conditions acted together to support rapid intensification.

4.4 Limitations and Implications for the Southwest Pacific

This study relies on a combination of satellite observations, ocean reanalysis products, and high-resolution model simulations to reconstruct the oceanic response associated with TC Winston. Although validation against Argo profiles and reef temperature observations indicates that the datasets realistically represent regional thermal conditions, uncertainties remain in the representation of mixed-layer processes and subsurface heat redistribution during extreme events. Global Argo observations indicate that tropical cyclones commonly produce substantial mixed-layer deepening and strong upper-ocean mixing (Han et al., 2025). Because ERA5 does not explicitly resolve many of the small-scale turbulent processes responsible for cyclone-induced entrainment, the MLD response diagnosed here may represent a conservative estimate of the actual upper-ocean adjustment. These limitations reflect a broader challenge across the Small Island States in the South Pacific, where subsurface ocean observations remain sparse and operational monitoring relies heavily on SST products. Our results demonstrate that the most significant oceanic changes associated with rapid intensification occurred beneath the mixed layer, highlighting the importance of upper-ocean stratification and subsurface heat content that cannot be resolved from SST alone (Leipper & Volgenau, 1972). The framework developed here provides a practical approach for investigating MHW–TC interactions in data-limited Pacific Island regions

and underscores the need for enhanced upper-ocean observing systems to improve understanding and prediction of tropical cyclone intensity change.

5. Summary

This study examined the oceanic mechanisms linking the 2016 southwest Pacific MHW to the rapid intensification of TC Winston. The results show that the MHW did not simply increase SSTs but fundamentally altered the vertical structure of the upper ocean. Enhanced radiative forcing and weak winds produced a shallow, strongly stratified mixed layer that facilitated the accumulation of heat within the upper ocean. Heat-budget diagnostics indicate that a substantial fraction of this energy was redistributed beneath the mixed layer, generating a vertically structured thermal reservoir that extended into the upper thermocline. The role of stratification was therefore primarily to promote heat storage and retention during the MHW development phase. During rapid intensification, cyclone-induced mixing progressively eroded this preconditioned structure and mobilized heat from throughout the upper ocean, extending well below the pre-storm mixed-layer depth. The strongest heat-content depletion occurred within subsurface reservoirs, indicating that the energetically important oceanic response was concentrated beneath the mixed layer. These suggest that upper-thermocline warming played a critical role in sustaining air–sea energy exchange during intensification. Rapid intensification was strongest when elevated subsurface heat availability (depleted 100% of THCP during RI3), sustained turbulent heat transfer, and weak vertical wind shear occurred simultaneously. This study therefore demonstrate that MHWs influence TC intensity not only through increased heat content, but through modification of the vertical distribution and accessibility of stored ocean heat.

More broadly, this study highlights the importance of subsurface ocean observations in the southwest Pacific, where observational constraints remain substantial. Because the key oceanic processes associated with Winston's intensification occurred beneath the mixed layer, reliance on sea-surface temperature alone may underestimate the contribution of marine heatwaves to tropical cyclone intensification. Improved monitoring of upper-ocean thermal structure and stratification will therefore be essential for understanding and forecasting future compound marine heatwave–tropical cyclone extremes in Pacific Island regions.

References

Alexander, M. A., Scott, J. D., & Deser, C. (2000). Processes that influence sea surface temperature and ocean mixed layer depth variability in a coupled model. *Journal of Geophysical Research: Oceans*, 105(C7), 16823–16842. https://doi.org/10.1029/2000JC900074

Balaguru, K., Chang, P., Saravanan, R., Leung, L. R., Xu, Z., Li, M., & Hsieh, J.-S. (2012). Ocean barrier layers' effect on tropical cyclone intensification. *Proceedings of the National Academy of Sciences, 109*(36), 14343–14347. https://doi.org/10.1073/pnas.1201364109

Balaguru, K., Foltz, G. R., Leung, L. R., Asaro, E. D., Emanuel, K. A., Liu, H., & Zedler, S. E. (2015). Dynamic potential intensity: An improved representation of the ocean's impact on tropical cyclones. *Geophysical Research Letters, 42*(16), 6739–6746. https://doi.org/10.1002/2015GL064822

Barnes, C. E., & Barnes, G. M. (2014). Eye and eyewall traits as determined with the NOAA WP-3D lower-fuselage radar. *Monthly Weather Review, 142*(9), 3393–3417. https://doi.org/10.1175/MWR-D-13-00375.1

Choi, H. Y., Park, M. S., Kim, H. S., & Lee, S. (2024). Marine heatwave events strengthen the intensity of tropical cyclones. *Communications Earth & Environment, 5*(1), 151. https://doi.org/10.1038/s43247-024-01239-4

de Boyer Montégut, C., Madec, G., Fischer, A. S., Lazar, A., & Iudicone, D. (2004). Mixed layer depth over the global ocean: An examination of profile data and a profile-based climatology. *Journal of Geophysical Research: Oceans, 109*(C12), C12003. https://doi.org/10.1029/2004JC002378

du Plessis, M. D., Nicholson, S. A., Giddy, I., Monteiro, P. M. S., Prend, C. J., & Swart, S. (2026). Southern Ocean summer warming is regulated by storm-driven mixing. *Nature Geoscience, 19*(1), 75–83. https://doi.org/10.1038/s41561-025-01857-3

DeMaria, M. (2009). A simplified dynamical system for tropical cyclone intensity prediction. *Monthly Weather Review*, *137*(1), 68–82. https://doi.org/10.1175/2008MWR2513.1

DeMaria, M., & Kaplan, J. (1994). A Statistical Hurricane Intensity Prediction Scheme (SHIPS) for the Atlantic Basin. *Weather and Forecasting*, *9*(2). https://doi.org/10.1175/1520-0434(1994)009<0209:ASHIPS>2.0.CO;2

Dutheil, C., Lal, S., Lengaigne, M., Cravatte, S., Menkès, C., Receveur, A., Börgel, F., Gröger, M., Houlbreque, F., Le Gendre, R., Mangolte, I., Peltier, A., & Meier, H. E. M. (2024). The massive 2016 marine heatwave in the Southwest Pacific: An El Niño–Madden-Julian Oscillation compound event. *Science Advances, 10*(49), eadp2948. https://doi.org/10.1126/sciadv.adp2948

Elzahaby, Y., & Schaeffer, A. (2019). Observational insight into the subsurface anomalies of marine heatwaves. *Frontiers in Marine Science, 6*,745. https://doi.org/10.3389/fmars.2019.00745

Emanuel, K. A. (1986). An air–sea interaction theory for tropical cyclones. Part I: Steady-state maintenance. *Journal of the Atmospheric Sciences, 43*(6), 585–605. https://doi.org/10.1175/1520-0469(1986)043<0585:AASITF>2.0.CO;2

Emanuel, K. A. (1999). Thermodynamic control of hurricane intensity. *Nature, 401*(6754), 665–669. https://doi.org/10.1038/44326

Emanuel, K., & Nolan, D. S. (2004). Tropical cyclone activity and the global climate system. *Journal of Geophysical Research: Atmospheres, 107*(D9–10), 1–9. https://doi.org/10.1029/2001JD001002

Esler, S. (2016). *Post-Disaster Needs Assessment – Tropical Cyclone Winston, February 20, 2016*. Fiji Government / World Bank.

Fairall, C. W., Bradley, E. F., Rogers, D. P., Edson, J. B., & Young, G. S. (1996). Bulk parameterization of air–sea fluxes for TOGA COARE. *Journal of Geophysical Research: Oceans, 101*(C2), 3747–3764. https://doi.org/10.1029/95JC03205

Frölicher, T. L., Fischer, E. M., & Gruber, N. (2018). Marine heatwaves under global warming. *Nature, 560*(7718), 360–364. https://doi.org/10.1038/s41586-018-0383-9

Garric, G., & Parent, L. (2016). *Global Ocean Reanalyses and Simulations: GLORYS2V4 product scientific and technical notice for users*. Mercator Ocean.

Goni, G. J., & Trinanes, J. A. (2003). Ocean thermal structure monitoring could aid in the intensity forecast of tropical cyclones. *Eos, Transactions American Geophysical Union, 84*(51), 573–578. https://doi.org/10.1029/2003EO510001

Granger, C. W. J. (1969). Investigating causal relations by econometric models and cross-spectral methods. *Econometrica, 37*(3), 424–438. https://doi.org/10.2307/1912791

Han, C., Bowen, M., & Sutton, P. (2025). Global observations of the response of the upper ocean to tropical cyclones based on Argo profiles. *Journal of Geophysical Research: Oceans, 130*(9), e2025JC022522. https://doi.org/10.1029/2025JC022522

Herry, N., Jullien, S., Vinour, L., Zribi, A., & Menkes, C. (2025). *A new reconstruction method for generating a realistic tropical cyclone wind field*. HAL preprint. https://hal.science/hal-05427687v1

Hersbach, H., Bell, B., Berrisford, P., Hirahara, S., Horányi, A., Muñoz-Sabater, J., Nicolas, J., Peubey, C., Radu, R., Schepers, D., Simmons, A., Soci, C., Abdalla, S., Abellan, X., Balsamo, G., Bechtold, P., Biavati, G., Bidlot, J., Bonavita, M., … Thépaut, J. N. (2020). The ERA5 global reanalysis. *Quarterly Journal of the Royal Meteorological Society, 146*(730), 1999–2049. https://doi.org/10.1002/qj.3803

Hirata, H., Kawamura, R., & Nonaka, M. (2025). Effects of a marine heatwave associated with the Kuroshio Extension large meander on extreme precipitation in September 2023. *Scientific Reports, 15*(1), 6821. https://doi.org/10.1038/s41598-025-88294-9

Hobday, A. J., Alexander, L. V., Perkins, S. E., Smale, D. A., Straub, S. C., Oliver, E. C. J., Benthuysen, J. A., Burrows, M. T., Donat, M. G., Feng, M., Holbrook, N. J., Moore, P. J., Scannell, H. A., Sen Gupta, A., & Wernberg, T. (2016). A hierarchical approach to defining marine heatwaves. *Progress in Oceanography, 141*, 227–238. https://doi.org/10.1016/j.pocean.2015.12.014

Hobday, A. J., Oliver, E. C. J., Sen Gupta, A., Benthuysen, J. A., Burrows, M. T., Donat, M. G., Holbrook, N. J., Moore, P. J., Thomsen, M. S., Wernberg, T., & Smale, D. A. (2018). Categorizing and naming marine heatwaves. *Oceanography, 31*(2), 162–173. https://doi.org/10.5670/oceanog.2018.205

Holbrook, N. J., Hernaman, V., Koshiba, S., Lako, J., Kajtar, J. B., Amosa, P., & Singh, A. (2022). Impacts of marine heatwaves on tropical western and central Pacific Island nations and their communities. *Global and Planetary Change, 208*, 103680. https://doi.org/10.1016/j.gloplacha.2021.103680

Holbrook, N. J., Scannell, H. A., Sen Gupta, A., Benthuysen, J. A., Feng, M., Oliver, E. C. J., Alexander, L. V., Burrows, M. T., Donat, M. G., Hobday, A. J., Moore, P. J., Perkins-Kirkpatrick, S. E., Smale, D. A., Straub, S. C., & Wernberg, T. (2019). A global assessment of marine heatwaves and their drivers. *Nature Communications, 10*(1), 2624. https://doi.org/10.1038/s41467-019-10206-z

Holbrook, N. J., Sen Gupta, A., Oliver, E. C. J., Hobday, A. J., Benthuysen, J. A., Scannell, H. A., Smale, D. A., & Wernberg, T. (2020). Keeping pace with marine heatwaves. *Nature Reviews Earth & Environment, 1*(9), 482–493. https://doi.org/10.1038/s43017-020-0068-4

Huang, B., Liu, C., Banzon, V., Freeman, E., Graham, G., Hankins, B., Smith, T., & Zhang, H.-M. (2021). Improvements of the Daily Optimum Interpolation Sea Surface Temperature (DOISST) version 2.1. *Journal of Climate, 34*(8), 2923–2939. https://doi.org/10.1175/JCLI-D-20-0806.1

IPCC. (2021). *Climate Change 2021: The Physical Science Basis*. Contribution of Working Group I to the Sixth Assessment Report of the Intergovernmental Panel on Climate Change (V. Masson-Delmotte et al., Eds.). Cambridge University Press. https://doi.org/10.1017/9781009157896

Jaimes, B., & Shay, L. K. (2015). Enhanced wind-driven downwelling flow in warm oceanic eddy features during the intensification of tropical cyclone Isaac (2012): Observations and theory. *Journal of Physical Oceanography, 45*(6), 1667–1689. https://doi.org/10.1175/JPO-D-14-0176.1

Knaff, J., & Sampson, C., (2009). Southern hemisphere tropical cyclone intensity forecast methods used at the Joint Typhoon Warning Center, Part II: statistical-dynamical forecasts. *Australian Meteorological and Oceanographic Journal*, *58*(1), 9–18. https://doi.org/https://doi.org/10.1071/ES09002

Kerry, C., Roughan, M., & De Souza, J. (2023). Characterizing the variability of boundary currents and ocean heat content around New Zealand using a multi-decadal high-resolution regional ocean model. *Journal of Geophysical Research: Oceans, 128*(4), e2022JC018624. https://doi.org/10.1029/2022JC018624

Knapp, K. R., Kruk, M. C., Levinson, D. H., Diamond, H. J., & Neumann, C. J. (2010). The International Best Track Archive for Climate Stewardship (IBTrACS). *Bulletin of the American Meteorological Society, 91*(3), 363–376. https://doi.org/10.1175/2009BAMS2755.1

Large, W. G., McWilliams, J. C., & Doney, S. C. (1994). Oceanic vertical mixing: A review and a model with a nonlocal boundary layer parameterization. *Reviews of Geophysics, 32*(4), 363–403. https://doi.org/10.1029/94RG01872

Le Gendre, R., Varillon, D., Fiat, S., Hocdé, R., N'Yeurt, A. de R., Andréfouët, S., Aucan, J., Cravatte, S., Duphil, M., Ganachaud, A., Gaudron, B., Kestenare, E., Liao, V., Pelletier, B., Peltier, A., Schaefer, A. L., Trophime, T., Van Wynsberge, S., Dandonneau, Y., …

Menkes, C. (2025). ReefTEMPS: The Pacific Islands coastal temperature network. *Earth System Science Data, 17*(10), 5277–5301. https://doi.org/10.5194/essd-17-5277-2025

Leipper, D. F., & Volgenau, D. (1972). Hurricane heat potential of the Gulf of Mexico. *Journal of Physical Oceanography*, 2(3), 218–224. https://doi.org/10.1175/1520-0485(1972)002<0218:HHPOTG>2.0.CO;2

Li, X., Zhan, R., Wang, Y., & Xu, J. (2021). Factors controlling tropical cyclone intensification over the marginal seas of China. *Frontiers in Earth Science, 9*, 795186. https://doi.org/10.3389/feart.2021.795186

Lin, I. I., Chen, C. H., Pun, I. F., Liu, W. T., & Wu, C. C. (2009). Warm ocean anomaly, air–sea fluxes, and the rapid intensification of tropical cyclone Nargis (2008). *Geophysical Research Letters, 36*(3), L03817. https://doi.org/10.1029/2008GL035815

Lin, I. I., Goni, G. J., Knaff, J. A., Forbes, C., & Ali, M. M. (2013). Ocean heat content for tropical cyclone intensity forecasting and its impact on storm surge. *Natural Hazards, 66*(3), 1481–1500. https://doi.org/10.1007/s11069-012-0214-5

McDougall, T. J., & Barker, P. M. (2011). *Getting started with TEOS-10 and the Gibbs Seawater (GSW) Oceanographic Toolbox*. SCOR/IAPSO WG127.

McGree, S., Smith, G., Chandler, E., Harold, N., Begg, Z., Kuleshov, Y., Malsale, P., & Ritman, M. (2023). *Climate Change in the Pacific 2022: Historical and recent variability, extremes and change*. Pacific Community (SPC).

Moisan, J. R., & Niiler, P. P. (1998). The seasonal heat budget of the North Pacific: Net heat flux and heat storage rates (1950–1990). *Journal of Physical Oceanography, 28*(12), 2327–2342. https://doi.org/10.1175/1520-0485(1998)028%3C0401:TSHBOT%3E2.0.CO;2

Nguyen, T. K. D., & Hsu, P. C. (2025). Dual effects of marine heatwaves on typhoon intensity and associated heat dissipation. *Remote Sensing, 17*(6), 968. https://doi.org/10.3390/rs17060968

Oliver, E. C. J., Benthuysen, J. A., Bindoff, N. L., Hobday, A. J., Holbrook, N. J., Mundy, C. N., & Perkins-Kirkpatrick, S. E. (2017). The unprecedented 2015/16 Tasman Sea marine heatwave. *Nature Communications, 8*, 16101. https://doi.org/10.1038/ncomms16101

Oliver, E. C. J., Benthuysen, J. A., Darmaraki, S., Donat, M. G., Hobday, A. J., Holbrook, N. J., Schlegel, R. W., & Sen Gupta, A. (2025). Marine heatwaves. *Annual Review of Marine Science, 17*, 301–328. https://doi.org/10.1146/annurev-marine-032720-095144

Oliver, E. C. J., Donat, M. G., Burrows, M. T., Moore, P. J., Smale, D. A., Alexander, L. V., Benthuysen, J. A., Feng, M., Sen Gupta, A., Hobday, A. J., Holbrook, N. J., Perkins-Kirkpatrick, S. E., Scannell, H. A., Straub, S. C., & Wernberg, T. (2018). Longer and more frequent marine heatwaves over the past century. *Nature Communications, 9*(1), 1324. https://doi.org/10.1038/s41467-018-03732-9

Paulson, C. A., & Simpson, J. J. (1977). Irradiance measurements in the upper ocean. *Journal of Physical Oceanography, 7*(6), 952–956. https://doi.org/10.1175/1520-0485(1977)007%3C0952:IMITUO%3E2.0.CO;2

Price, J. F. (1981). Upper ocean response to a hurricane. *Journal of Physical Oceanography, 11*(2), 153–175. https://doi.org/10.1175/1520-0485(1981)011%3C0153:UORTAH%3E2.0.CO;2

Pun, I.-F., Lin, I.-I., & Wu, C.-C. (2025). Suppression of marine heatwave activity by tropical cyclone-induced upper ocean cooling. *Science Advances, 11*(46), eadw8070. https://doi.org/10.1126/sciadv.adw8070

Radfar, S., Foroumandi, E., Moftakhari, H., Moradkhani, H., Foltz, G. R., & Sen Gupta, A. (2024). Global predictability of marine heatwave induced rapid intensification of tropical cyclones. *Earth's Future, 12*(12), e2024EF004935. https://doi.org/10.1029/2024EF004935

Rathore, S., Goyal, R., Jangir, B., Ummenhofer, C. C., Feng, M., & Mishra, M. (2022). Interactions between a marine heatwave and tropical cyclone Amphan in the Bay of Bengal in 2020. *Frontiers in Climate, 4*, 861477. https://doi.org/10.3389/fclim.2022.861477

Rogers, R., Reasor, P., & Lorsolo, S. (2013). Airborne Doppler observations of the inner-core structural differences between intensifying and steady-state tropical cyclones. *Monthly Weather Review, 141*(9), 2970–2991. https://doi.org/10.1175/MWR-D-12-00357.1

Runge, J., Bathiany, S., Bollt, E., Camps-Valls, G., Coumou, D., Deyle, E., Glymour, C., Kretschmer, M., Mahecha, M. D., Muñoz-Marí, J., van Nes, E. H., Peters, J., Quax, R., Reichstein, M., Scheffer, M., Schölkopf, B., Spirtes, P., Sugihara, G., Sun, J., … Zscheischler, J. (2019). Inferring causation from time series in Earth system sciences. *Nature Communications, 10*(1), 2553. https://doi.org/10.1038/s41467-019-10105-3

Scannell, H. A., & McPhaden, M. J. (2018). Seasonal mixed layer temperature balance in the southeastern tropical Atlantic. *Journal of Geophysical Research: Oceans, 123*(8), 5557–5570. https://doi.org/10.1029/2018JC014099

Schlegel, R. W., & Smit, A. J. (2018). heatwaveR: A central algorithm for the detection of heatwaves and cold-spells. *Journal of Open Source Software, 3*(27), 821. https://doi.org/10.21105/joss.00821

Schlegel, R. W., Oliver, E. C. J., & Chen, K. (2021). Drivers of marine heatwaves in the Northwest Atlantic: The role of air–sea interaction during onset and decline. *Frontiers in Marine Science, 8*, 627970. https://doi.org/10.3389/fmars.2021.627970

Shay, L. K., Goni, G. J., & Black, P. G. (2000). Effects of a warm oceanic feature on Hurricane Opal. *Monthly Weather Review, 128*(5), 1366–1383. https://doi.org/10.1175/1520-0493(2000)128%3C1366:EOAWOF%3E2.0.CO;2

Shen, W., & Ginis, I. (2003). Effects of surface heat flux-induced sea surface temperature changes on tropical cyclone intensity. *Geophysical Research Letters*, *30*(18). https://doi.org/10.1029/2003GL017878

Vincent, E. M., Emanuel, K. A., Lengaigne, M., Vialard, J., & Madec, G. (2015). Influence of upper ocean stratification interannual variability on tropical cyclones. *Journal of Advances in Modeling Earth Systems, 6*(3), 680–699. https://doi.org/10.1002/2014MS000327

Vincent, E. M., Madec, G., Lengaigne, M., Vialard, J., & Koch-Larrouy, A. (2013). Influence of tropical cyclones on sea surface temperature seasonal cycle and ocean heat transport. *Climate Dynamics, 41*(7–8), 2019–2038. https://doi.org/10.1007/s00382-012-1556-0

Zhang, Z., Wang, W., Doyle, J. D., Moskaitis, J., Komaromi, W. A., Heming, J., Magnusson, L., Cangialosi, J. P., Cowan, L., Brennan, M., Ma, S., Das, A. K., Takuya, H., Clegg, P., Birchard, T., Knaff, J. A., Kaplan, J., Mohapatra, M., Sharma, M., … Blake, E. (2023). A review of recent advances (2018–2021) on tropical cyclone intensity change from operational perspectives, part 1: Dynamical model guidance. *Tropical Cyclone Research and Review*, *12*(1), 30–49. https://doi.org/10.1016/j.tcrr.2023.05.004